This manuscript is a preprint:

This manuscript has been submitted to Tectonics. Subsequent versions of this manuscript may have different content. If accepted, the final version of this manuscript will be available via the 'Peer-reviewed Publication DOI' link via this webpage.

Please feel free to contact any of the authors directly or to comment on the manuscript. We welcome feedback!

Interplay between geometry and brittle deformation of bedrock fault scarps

B. J. Andrews[1], Constanza Rodriguez Piceda[1], and D.C.P. Peacock[2], Z. K. Mildon[1]

1) School of Geography, Earth and Environmental Sciences, University of Plymouth, Drake Circus, Plymouth, PL4 8AA, UK

2) Department of Geology, Hull University, Hull, HU6 7RX, United Kingdom

Corresponding author: Billy J. Andrews (billy.andrews@plymouth.ac.uk)

Key Points:

- Brittle deformation of the fault core accounts for a portion of an earthquake's energy budget, but how this varies is poorly constrained.
- We study how faults and fractures vary along two fault scarps in Malta to quantify spatial-temporal variations in brittle deformation.
- Fracture intensity and geometry correlate with fault-plane geometry, and cross-faults rotate fractures and the fault scarp.

Key words

Earthquakes, Active faults, Fracture networks, Energy budget, Seismic Hazard, Fault core

Abstract

Energy built up during interseismic phases is released during earthquakes as seismic energy and dissipated within fault zones. Seismological observations indicate spatial variations in earthquake behavior across a fault (e.g., rupture speed, stress drop, wave directivity). However, how this relates to energy dissipation through brittle fracturing in the fault zone is difficult to quantify from seismological observations. Spatial patterns of on-fault fractures across two bedrock normal fault scarps in Malta are investigated, with fracture network properties related to identified cross-faults and changes in fault-plane geometry. Cross-faults (i.e., faults that offset the main plane) are common across both faults, with throws from 0.2 to 14 m. On-fault fractures are commonly en echelon and contribute to a connected fracture network. The orientation, intensity and connectivity of on-fault fractures display spatial changes associated both with proximity to cross-faults and changes in fault-plane geometry (e.g., corrugations). On-fault fracture and corrugation trends are block rotated by 10˚ to 40˚ by cross-fault zones, indicating corrugations and some on-fault fractures pre-date cross-faults. The elevated fracture intensity and connectivity adjacent to cross-faults, and the sharp contrast in fracture properties across them, indicate that on-fault fractures continued to develop during or after cross-fault formation. This suggests cross-faults are an energy sink during earthquake slip, reducing radiation efficiency and possibly promoting rupture arrest. This observation indicates interaction between the cross-faults and the main fault at surface, and suggests cross-faults play a significant role in earthquake energy dissipation in the shallow sub-surface.

Plain Language Summary

During an earthquake, the energy that has built up on a fault is released during an earthquake, potentially leading to extensive damage and/or loss of life. Only part of this energy is radiated as seismic waves with a substantial proportion dissipated within the fault zone through frictional heating and the breakdown of rock to create subsidiary faults and fractures. How energy is partitioned controls rupture behaviour and ground shaking intensity, however, the spatial variability of energy dissipation remains poorly understood.

To investigate this, we mapped fault plane geometry, cross-cutting faults, and on-fault fractures across two normal fault scarps in Malta. We find that on-fault damage is highly heterogeneous with fracture intensity, length, and network connectivity vary systematically along strike, increasing near bends in the fault surface. Cross-faults form through the progressive localization of strain within the on-fault fracture network. Cross-faults rotate the fault plane and pre-existing fractures and localise the development of new fractures, producing abrupt step-changes in fracture properties. Our findings demonstrate that geometric heterogeneities and cross-faults strongly effect on-fault damage, and that mapping these features prvides key insights into the energy budget during shallow earthquake slip.

1 Introduction

The total elastic strain energy ($\boldsymbol{E_{total}}$) accumulated during the interseismic phase caused by tectonic loading is released during earthquakes and/or aseismic slip. However, only part of this energy is converted into seismic radiation. The energy budget, which ultimately controls rupture dynamics and the amount of radiated seismic energy, can be expressed as:

$$\boldsymbol{E_{total} = E_R + E_G + E_{Th}}$$

where $\boldsymbol{E_R}$ is the radiated energy through seismic waves, $\boldsymbol{E_G}$ is the fracture energy required for rupture propagation, leading to the production of fault rocks and fractures, and $\boldsymbol{E_{Th}}$ is the energy dissipated within the fault zone through frictional heating (Ide, 2002; Kanamori & Rivera, 2006; Nielsen et al., 2016). The ratio of the radiated energy $\boldsymbol{E_R}$ to that energy dissipated during rupture propagation and within the fault zone ($\boldsymbol{E_G + E_{Th}}$) is referred to as the radiation efficiency, which is derived from seismological sources (Beeler et al., 2003; Savage & Wood, 1971; Shearer, 2019). Earthquakes with low radiation efficiency, where a high proportion of energy is dissipated within the fault zone, result in reduced ground shaking compared to earthquakes with high radiation efficiency in faults of similar size and tectonic loading history (e.g., Kanamori, 2001). Therefore, understanding how energy dissipation varies both between and across active faults is crucial for the assessment of the seismic hazard they pose.

Seismological observations indicate large along-strike and down-dip variability in rupture speed, stress drop, and radiation efficiency for a given earthquake (e.g., Fletcher & McGarr, 2006). This suggests that energy dissipation varies along a fault's length, making it important to consider energy dissipation at a given point on the fault (Cocco et al., 2023; Nielsen et al., 2016).

Faults are not single planar surfaces but rather fault zones consisting of one or more fault cores, where the majority of strain is accommodated, surrounded by a damage zone (Caine et al., 1996; Choi et al., 2016; Kim et al., 2004). Energy dissipated within the fault zone may therefore either be on-fault (i.e., within the fault core), or off-fault (e.g., creation of new fractures or shear along existing structures such as antithetic or synthetic faults within the damage zone (Cocco et al., 2023; Nielsen et al., 2016)). Coseismic off-fault damage can reduce the radiation efficiency of earthquakes on a fault when compared to scenarios where slip is confined to the fault core (Cocco et al., 2023; De Paola et al., 2025; Huang, 2018; Okubo et al., 2019; Thomas et al., 2017). Non-planar fault geometries such as fault bends and fault segmentation, which are oten referred to as geometrical complexities, have been shown to promote additional off-fault damage (Okubo et al., 2019; Rodriguez Padilla et al., 2024). The role non-planar geometries and fault segmentation has on the distribution of on-fault energy sinks is challenging to deduce due to resolution limitations of seismological methods, making small-scale stress-drop variations along a fault surface difficult to detect.

Fault segmentation and non-planar geometries that affect the energy budget can be identified through field studies of exhumed faults (e.g., Barth et al., 2013; Chester & Chester, 2000; Chester et al., 2005; Faulkner et al., 2003; Shipton et al., 2006). Most of the faults described in those papers have, however, undergone multiple deformation phases (e.g., reactivation an/or uplift and exhumation), complicating the distinction between features that formed during earthquakes and those resulting from exhumation processes. One way to overcome this is through deep borehole studies (e.g., the San Andreas Fault Observatory at Depth (SAFOD) borehole) which provide direct insights into fault structure at depth (Bradbury et al., 2011;

Holdsworth et al., 2011). Borehole studies are costly and only sample a very small section of the fault, therefore, extrapolating these data carries considerable uncertainities given the significant spatial heterogeneity observed across fault zones (De Rosa et al., 2018; L. McKay et al., 2021; Lucy McKay et al., 2019; Torabi et al., 2019). It is therefore difficult to deduce how fault zone structure may affect along-strike changes in radiation efficiency at depth from current datasets.

Fracture development is an important energy sink in the shallow crust (Nielsen et al., 2016; Shearer, 2019), and can develop both on the fault plane and within a damage zone. On-fault fractures (i.e., fractures on the slip-surface) are abundant across bedrock fault scarps of active normal faults (Chester & Chester, 2000; Friedman & Logan, 1970; Hancock & Barka, 1987; Lacazette, 2009; Smeraglia et al., 2017; Stewart & Hancock, 1990). Cross-faults (i.e., faults that occur at a high angle to, and cross the trend of, principle faults in an actively deforming region) have been identified as playing an important role in shallow earthquake slip. Examples include the 1987 Supersitition Hills earthquake sequence in California (Hudnut et al., 1989; Larsen et al., 1992), the 1992 Big Bear and Landers, California, earthquakes (Jones & Hough, 1995), the 2010 Darfield earthquake in New Zealand (Barnhart et al., 2011; Elliott et al., 2012), the 2010-2011 Rigan earthquake sequence in Iran (Rezapour & Mohsenpur, 2013; Walker et al., 2013), the 2012 Sumatra earthquake (Meng et al., 2012; Wei et al., 2013), and 2019 Ridgecrest, California (Barnhart et al., 2019; Ponti et al., 2020). Cross-cutting pre-existing faults can act as barriers to rupture propagation. For example, an inherited Miocene-Pliocene thrust ramp is suggested as a barrier to the propagation of the first two earthquakes of the 2016 Central Italy Sequence (24th August, Mw 6.0 and 26th October, Mw 5.9), leading to a stress concentration on the pre-existing

fault that acted as the nucleation zone of the third and most powerful earthquake in the sequence (30th October, Mw 6.5) (Pizzi et al., 2017).

Bedrock fault scarps associated with active or recently active faults provide an ideal setting for systematically studying earthquake energy dissipation through brittle fracturing, because 1) they have not been exhumed from great depth since faulting, 2) can be exposed across hundreds of meters, 3) display consistent fault zone structures, and 4) commonly cut by abundant cross-faults and on-fault fracture networks. We identify and quantify the properties of cross-faults and on-fault fractures to investigate consistent dissipative energy sinks and examine how these vary spatially across a fault plane, while also testing whether fault plane geometry influences the growth of on-fault fractures. To achieve this, we use drone-derived Digital Elevation Models (DEMs) of two bedrock fault scarps in Malta (the Victoria Lines and Maghlaq faults, Fig. 1) to document and compare variations in fault plane geometry with the presence of cross-faults (i.e., faults that offset the fault plane). The use of both fault scarps enabled us to compare cross-fault development between an isolated segment of the Victoria Lines Fault, and a portion of the Maghlaq Fault that is proposed to have formed through the linkage of several initially isolated segments. Furthermore, we compare changes in fault plane geometry along the Maghlaq Fault with the distribution of on-fault fractures mapped at a scale of 1:50. Our findings suggest that fault plane geometry influences on-fault fracture distributions, and that cross-faults cause the block-rotation of the fault plane at shallow depths. On-fault fractures continue to develop after cross-fault development, with jumps in fracture intensity observed either side of cross-faults, and an increase in on-fault fracture intensity close to cross-faults as they develop a damage zone. Our data suggests fault plane geometry and cross-faults influence energy

dissipation in the near surface, and represent an important contribution to the energy budget within the shallow sub-surface.

2. Geological setting

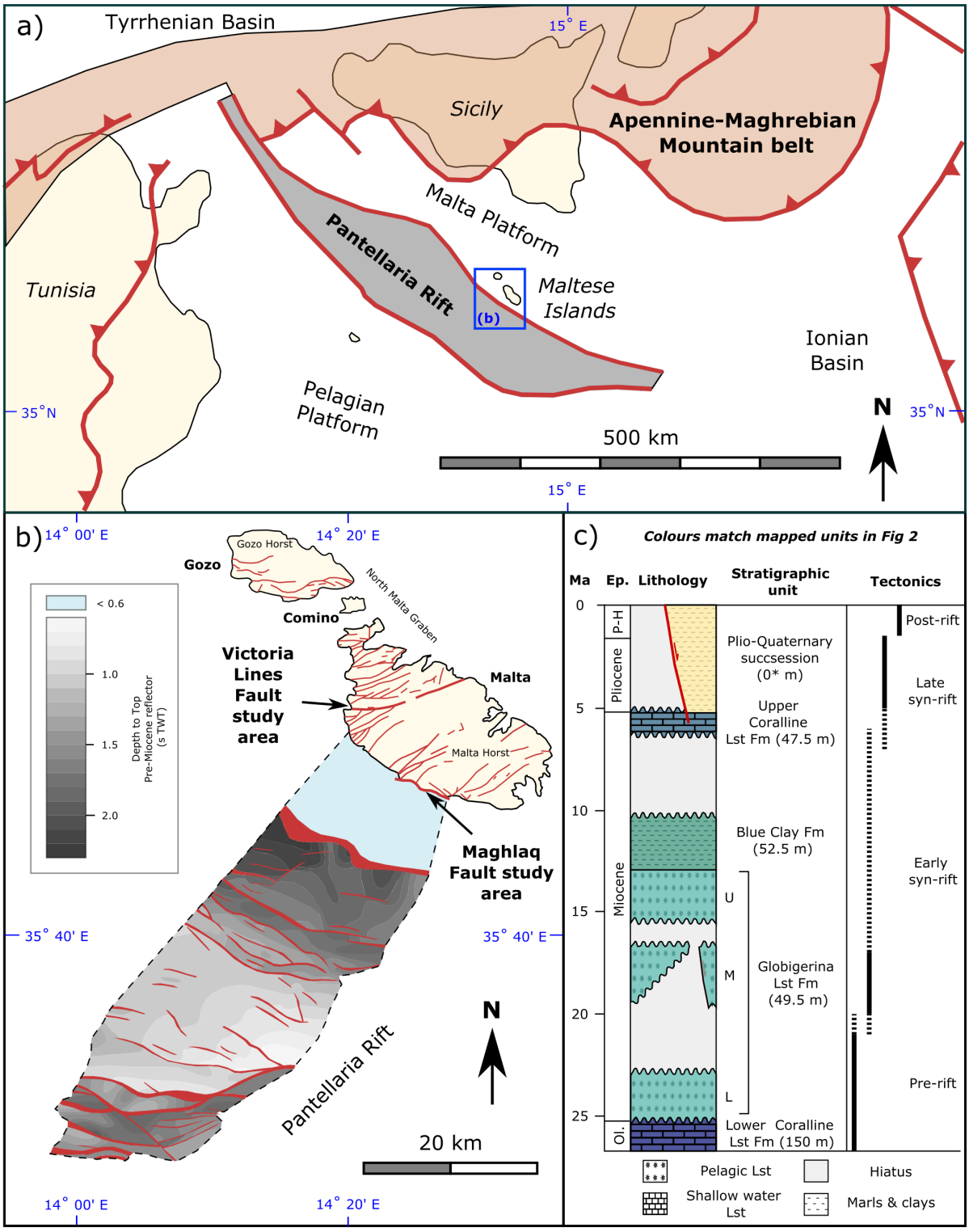

Figure 1: Geological setting of the Maltese Islands: a) Regional geology of the central Mediterranean showing the tectonic setting of the Maltese islands (after Dart et al., 1993). b)

Location of major normal faults in the Maltese islands and an offshore section of the Pantellaria Rift (after Bonson et al., 2007). c) Tectono-stratigraphic log of the Oligocene to Quaternary sediments of the Maltese archipelago (after Dart et al., 1993). The timings of the tectonic phases are taken from Dart et al, (1993) and Martinelli et al, (2019). The Maghlaq Fault represents the most north-easterly extent of the faults of the Pantellaria Rift, with faulting initiating at ~21 Ma and locally offsetting the Plio-Quaternary succession.

The Victoria Lines and Maghlaq Faults outcrop across the center and along the SW coast of Malta respectively (Fig 1a). The Maltese islands are located on the Pelagian Platform, which is on the foreland of the Apennine-Sicilian-Maghrebian orogenic belt (Argnani, 1990a; Dart et al., 1993; Hill & Hayward, 1988). The platform is cut by the ESE-WNW trending Pantelleria Rift system, also known as the Strait of Sicily Rift, which started opening in the late Miocene (Cello et al., 1985; Dart et al., 1993; Finetti, 1985; Reuther & Eisbacher, 1985). The rift system is composed of three ~NW-SE trending depocenters; the Pantelleria, Linosa, and Malta troughs (Reuther & Eisbacher, 1985). The late Oligocene to present tectonic evolution of the Pantelleria Rift resulted from the northward migration of the Apennine-Sicilian-Maghrebian orogenic belt (Argnani, 1990b; Dart et al., 1993).

Rifting caused two main sets of normal faults, trending WNW-ESE and ENE-WSW respectively, that offset the predominantly carbonate Oligo-Miocene stratigraphic succession (Dart et al., 1993; Illies, 1981; Reuther & Eisbacher, 1985). Whilst there is some debate upon the exact timings and kinematic details surrounding the structural evolution (e.g., Martinelli et al., 2019 *and references therein*), four tectono-sedimentary stages have been identified (Fig. 1b; Dart

et al., 1993): (i) pre-rift (>21 Ma); (ii) early syn-rift, extending from 21 to 6 Ma (Dart et al., 1993), or 20 to 17 Ma (Martinelli et al., 2019), characterized by minor faulting and dyke emplacement; (iii) late syn-rift, extending from ~5 to 1.5 Ma (Dart et al., 1993), or 7 to 1.5 Ma (Martinelli et al., 2019), characterised by major fault growth, and (iv) post-rift (<1.5 Ma). Kinematic analysis of faults on the Maltese Islands show that faults that formed during the early rift phase developed under a different stress field than those that developed during the late syn-rift phase (Martinelli et al., 2019). Early faults, which typically have <5 m throw, developed under oblate WNW-ESE extension (Martinelli et al., 2019). Faults during the late syn-rift phase show throws of up to 200

m, and include the regional fault sets on the Maltese Islands (e.g., Victoria Lines and Maghlaq faults) (Martinelli et al., 2019).

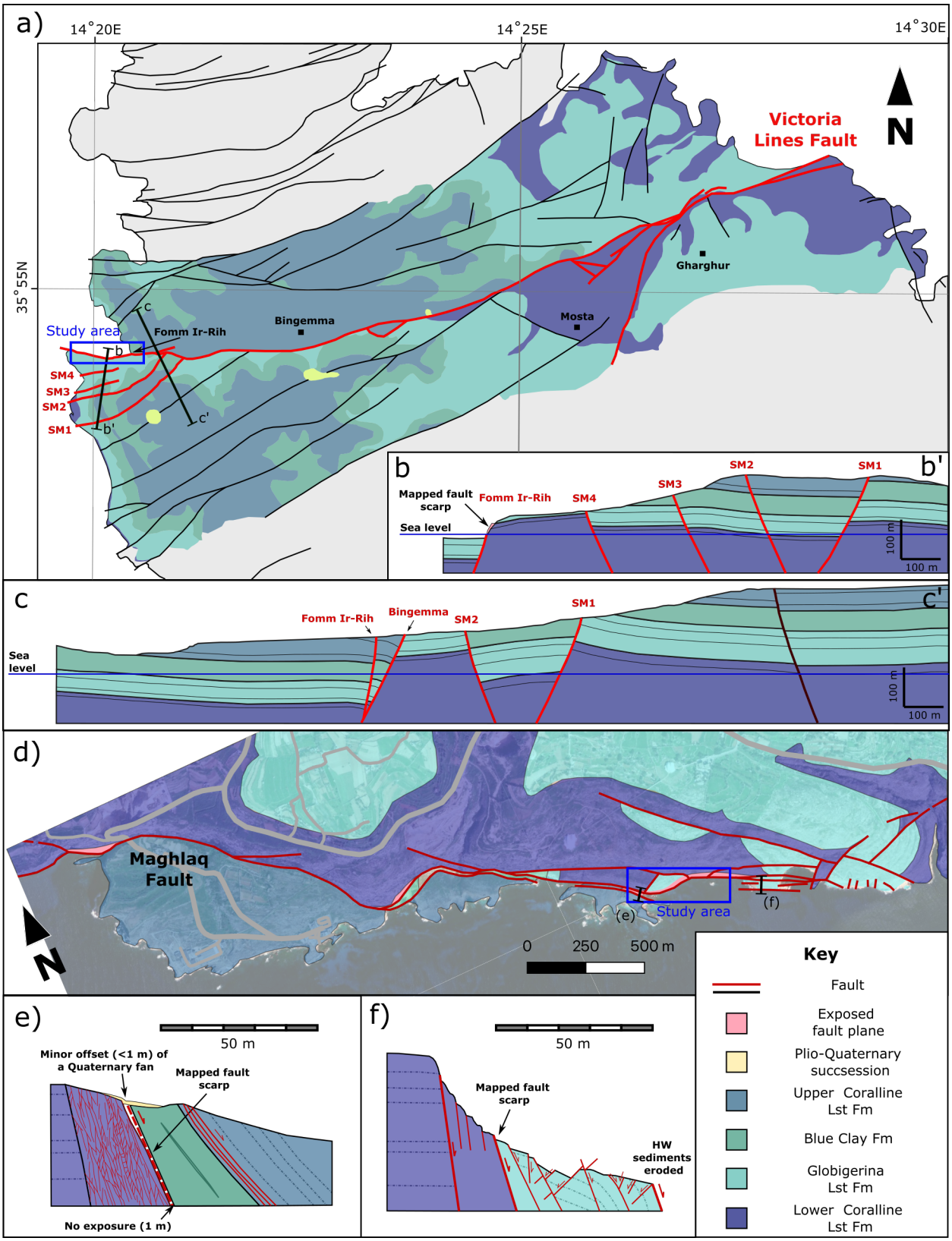
a)
14°20E
14°25E
14°30E
35°55N
N
Victoria
Lines Fault
Gharghur
Mosta
Bingemma
Fomm Ir-Rih
Study area
SM4
SM3
SM2
SM1
b
b'
c
c'
Mapped fault scarp
Sea level
100 m
Sea level
d)
Maghlaq
Fault
N
(e)
(f)
Study area
0
250
500 m
Key
Fault
Exposed fault plane
Plio-Quaternary succsession
Upper Coralline Lst Fm
Blue Clay Fm
Globigerina Lst Fm
Lower Coralline Lst Fm
e)
50 m
Minor offset (<1 m) of a Quaternary fan
Mapped fault scarp
No exposure (1 m)
f)
50 m
Mapped fault scarp
HW sediments eroded

186

Figure 2: Geological map and cross-sections of the Victoria Lines and Maghlaq Faults (after Villani et al. (2018) and Bonson et al. (2007) respectively). a) Geological map of the area surrounding the Victoria Lines Fault, showing the study area and location of cross-sections (b) and (c). (b-c) Cross-sections showing the throw distribution across the Fomm Ir-Rih and St. Martin fault segments of the Victoria Lines fault. d) geology of the area sorrounding the Maghlaq Fault showing the location of the study area and panels (e) and (f). (e-f) Cross-sections either side of the study area in the Maghlaq Fault.

The Victoria Lines Fault, also called the Great Fault (Putz-Perrier & Sanderson, 2010), extends for ~14 km across the center of Malta, creating a prominent escarpment that trends between 250° in the east and 270° in the west (Fig 1, 2a). The Victoria Lines Fault separates the North Malta Graben to the north from the Malta Horst to the south and has a maximum throw of ~195 m (Putz-Perrier & Sanderson, 2010). There is no evidence of Quaternary activity along the Victoria Lines Fault (Illies, 1981; Trechmann, 1938), with the last postulated movement based on seismic tomography profiles across the western extent of the fault being during the Middle Pleistocene (~0.6 Myr) (Villani et al., 2018). The Victoria Lines Fault is not a continuous fault, but is composed of multiple sub-parallel and overlapping strands, with some localized splay faults and branches in the westernmost and easternmost portions of the fault (Fig 2a-c) (Villani et al., 2018). Displacement in the western portion of the fault is accommodated across a few segments that include the 2.1 km-long Fomm Ir-Rih segment, four sub-ordinate NW- and SE- dipping splays termed the St. Martin Segments, and the ~4.6 km long Bingemma segment (Fig 2 a-c). This study focuses on the Fomm Ir-RiH segment, which displays a maximum throw of 119 m and decreases to near zero at the east of the study area (Fig 2c; Villani et al., 2018). The study area is a 1.2 km

long continuous coastal section (sea cliff) of a northerly dipping normal fault plane (Fig 2a), enabling along-strike patterns in cross-faults to be systematically studied across the fault segment. Because of weathering of the Victoria Lines Fault scarp, it was not possible to reliably map fractures at a consistent resolution across the study area. It was therefore decided that only cross-faults will be studied for the Victoria Lines Fault.

The Maghlaq Fault is located along the south-west coast of Malta, with the footwall of the fault exposed along a ~4 km continuous coastal section (Bonson et al., 2007). The trend of the Maghlaq Fault is ESE-WNW, matching fault orientations observed in the Pantelleria Rift to the south-west of Malta (Fig. 1) (Bonson et al., 2007; Pedley et al., 1976; Reuther & Eisbacher, 1985). Displacement probably started during the Messinian (7-5 Ma), with activity increasing after 5 Ma (Dart et al., 1993; Martinelli et al., 2019). Quaternary fans are offset in places by the Maghlaq Fault (Fig 2e), suggesting slip on the Maghlaq Fault continued for longer than the Victoria Lines Fault (Bonson et al., 2007). Despite seismicity being recorded in the Northern Pantelleria Rift, there is no direct evidence for neotectonic fault movements along the Maghlaq Fault (Bonson et al., 2007; Reuther & Eisbacher, 1985). Faulting across the exposed scarp likely occurred in to top few hundered meters, with the burial of the footwall sediments not exceeding 250 to 300 m (Bonson et al., 2007). The Maghlaq Fault consists of left-stepping, en echelon normal fault array striking ESE-WNW striking, with 60˚ dipping segments 1-2 km long (Fig 1; Bonson et al., 2007). Locally, these are joined by 10s to 100s m long fault segments that form fault bends, including our study area (Figure 2d-f) (Bonson et al., 2007). In our study area, a southerly dipping fault scarp is, similarly to the Victora Lines Fault, preserved over a continuous ~430 m coastal section. Unlike the Victoria Lines Fault segment, the Maghlaq Fault segment has

231 an exceptionally well exposed slip surfaces (Fig. S1-2), enabling on-fault fractures to be mapped
232 across the whole study area.

233 **3 Materials and Methods**

234 3.1 Quantifying fault plane geometry and inferring slip-vector

235 An unmanned aerial vehicle (drone) was used to capture imagery across the Victoria Lines
236 and Maghlaq fault scarps, ensuring a minimum 70% overlap between photographs to facilitate
237 photogrammetric processing, which was undertaken using the software Agisoft MetaShape to
238 create virtual outcrop models. From the virtual outcrop models, digital elevation models (DEM)
239 and orthomosaics were extracted and loaded into QGIS for analysis. The images for the Maghlaq
240 Fault covered sections of the fault with exceptional exposures of the fault scarp, extending ~430
241 m along strike and between ~4 and ~25 m down-dip. The Victoria Lines Fault model covered the
242 full extent of the Fomm Ir-RiH segment, extending ~1250 m along strike and between 5 and 19
243 m down dip.

244 The fault plane geometry was quantified, and slip-vectors inferred, from the DEM. Dip
245 and dip-direction maps were generated using the slope and aspect raster tools in QGIS.
246 Corrugations, used to infer slip vector, were inferred through the visual analysis of the dip-
247 direction map to map the location of down-dip ridges and troughs. These features were mapped,
248 using a minimum length of 0.4 m to reduce the effect of noise. The trend of the corrugation was

249 calculated in QGIS, and the dip was determined from calculating the slope of the linear regression
250 of the depth values extracted along the mapped corrugation.

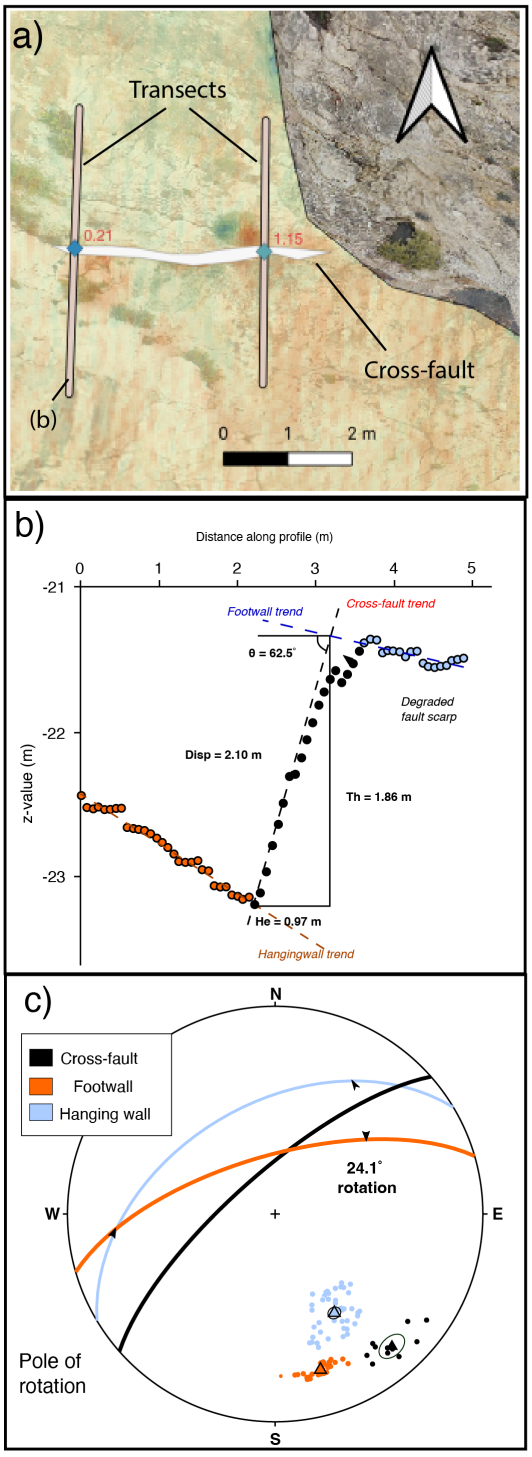

251

Figure 3: Quantification of cross-fault throw and rotation. a) Example transects used to extract cross-fault throw. b) Profile extracted from the DEM, highlighting how throw is measured; c) Stereographic projection of fault plane geometry extracted from the transect that is used to calculate scarp rotation using stereograph analysis.

Several cross-faults are observed along both the Victoria Lines and Maghlaq faults. These are mapped based on abrupt changes in dip-direction that coincide with a change in z-value on the DEM. Once mapped, fault-perpendicular transects, with sufficient density to capture along-stike changes in fault throw, were used to extract slope profiles across the fault. Profiles are then visually split into footwall (FW), hanging wall (HW), and fault plane subsections to calculate fault throw, heave, displacement and an estimation of fault dip (Fig. 3a). Additionally, these profiles are used to determine the fault plane geometry from the dip and dip direction maps with the mean orientation calculated for each subsection (HW, FW and Fault Plane) using Stereonet 10 (Fig 3b) (Allmendinger et al., 2013; Cardozo & Allmendinger, 2013). The angular rotation between the footwall and hanging wall, as well as the line of intersection, is calculated for each transect and compared to the extracted throw value (fig. 3b).

3.2 On-fault fracture mapping and fracture network analysis

Fracture networks were analyzed through lineament mapping in QGIS by a single interpreter, maintaining a constant scale of 1:50, and with snapping enabled to reduce subjective bias (Andrews et al., 2019). Features above a map-view length of ~0.05 to 0.1 m (~5-10 pixels) were mappable at this scale. Fracture type could not be reliably discerned, leading to all lineaments being mapped as a single layer. For lineaments wider than the pixel size (>0.02 m),

273 the fracture was digitized at its center, with connected fractures snapped onto the mapped
274 fracture. Although this method introduces a small uncertainty in the spatial location, the
275 magnitude of this uncertainty is low, thus not affecting comparisons between fracture properties
276 and fault plane geometry. Fracture aperture was not considered in this study, as the majority of

apertures fall below the pixel resolution of the orthomosaic and aperture may have been widened by weathering and erosion.

Following digitization, the map view trace length (Tl_{map}) and orientation of fractures were added to the attribute table in QGIS. An estimation of true trace length ($\mathrm{Tl}_{\mathrm{true}}$) is then calculated by considering the best-fit slope along the transect similarly to the calculation of cross-fault dip.

On-fault fracture trend (i.e., fault-fracture intersection lineation) was calculated using the start and end point of the polylines. Whilst this will induce small orientation errors for sinuous fractures, most digitized fractures had low sinuosity (average = 1.005), so should not affect the results presented here. For plotting purposes, the central points of fractures were chosen when displaying spatial trends in fracture orientation. An adapted gridded circular scanline method (after Mauldon et al., 2002) with a spacing of 0.2 m and a 1 m radius was used to investigate spatial distributions of fault scarp geometry, fracture intensity and fracture connectivity (See Supplementary 2 for further details). We then compared trends in fault scarp geometry, fracture intensity, and fracture connectivity to the presence of mapped cross-faults.

3 Results

3.1 Fault plane geometries and corrugation trends

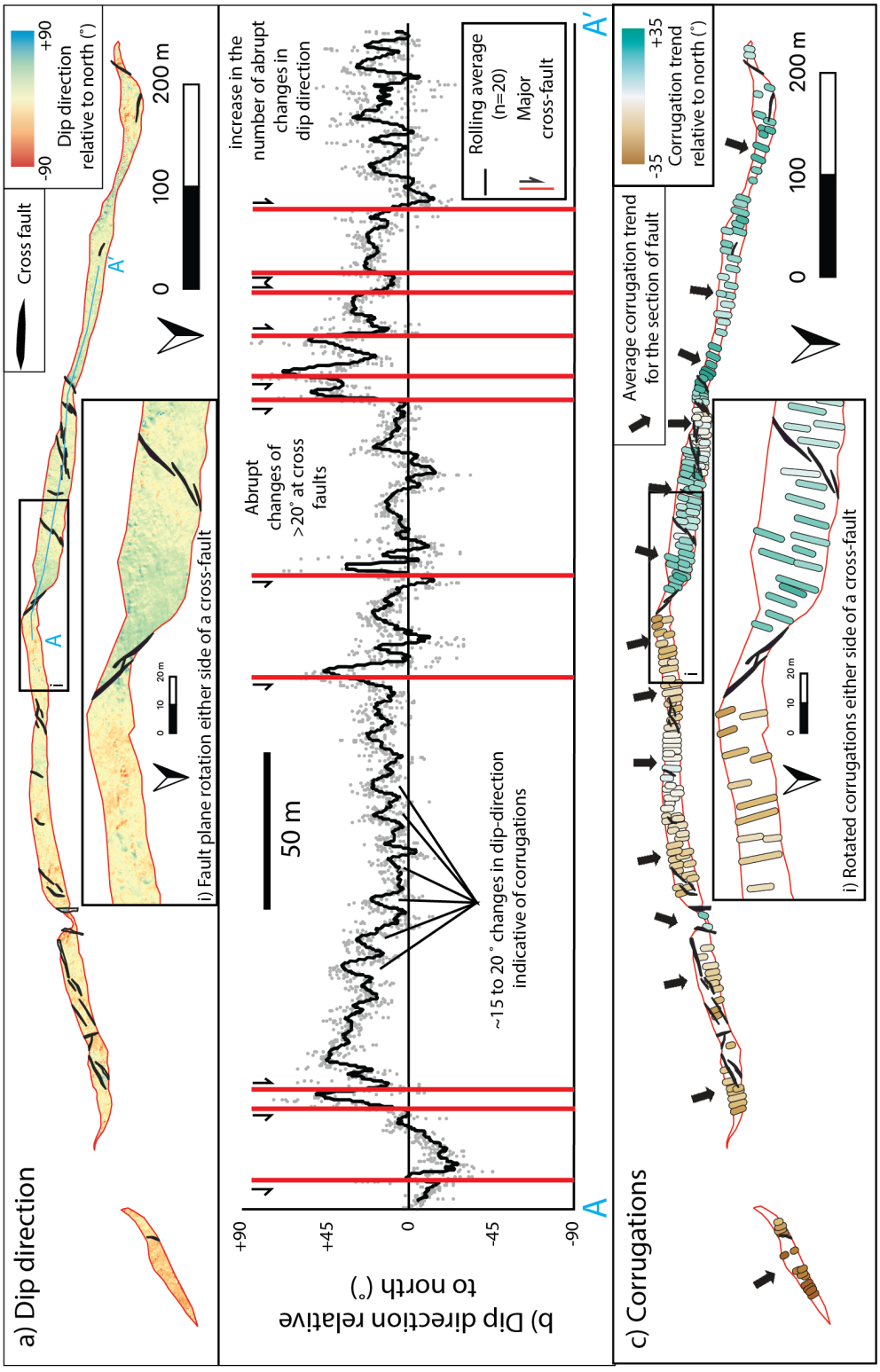

Figure 4: Fault plane geometry and corrugation trends for the Victoria Lines Fault. a) Dip-direction map highlighting the rotation of the fault plane either side of major cross-faults. b) Along-strike variation in dip-direction along the profile A-A', highlighting the changes in dip-direction used to map out corrugations and abrupt changes used to identify cross-faults. c) Map showing the trend of mapped corrugations across the Victoria Lines Fault. Black arrows indicate the average corrugation trend between prominent cross-faults. Note how corrugations converge towards the center of the study area, and are rotated across major cross faults (see sub-panel ci).

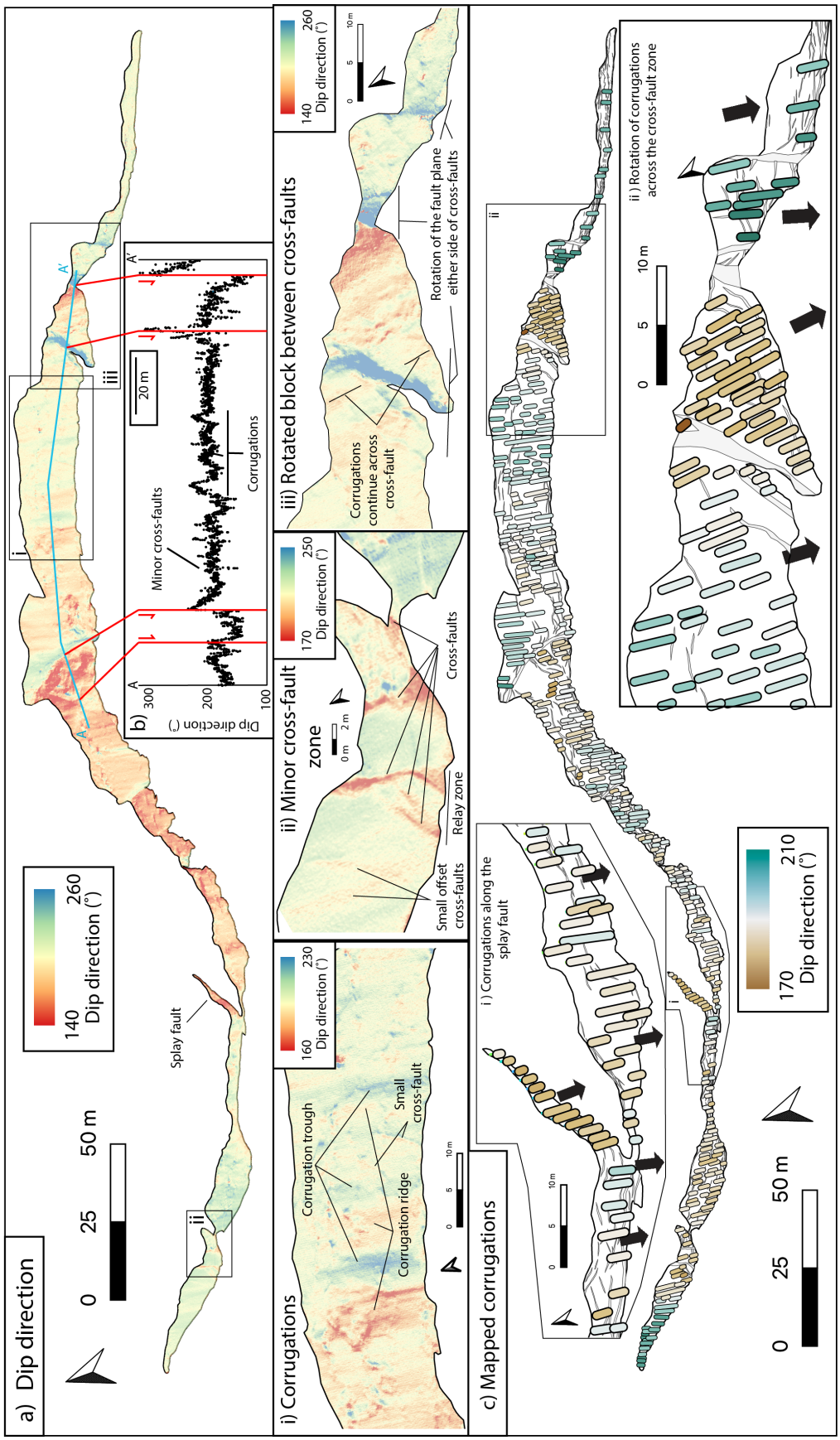
a) Dip direction
0
25
50 m
140
260
Dip direction (°)
Splay fault
A
A'
i
ii
iii
b)
Dip direction (°)
300
200
100
A
A'
20 m
Minor cross-faults
Corrugations
i) Corrugations
160
230
Dip direction (°)
Corrugation trough
Corrugation ridge
Small cross-fault
ii) Minor cross-fault zone
170
250
Dip direction (°)
0 m
2 m
Small offset cross-faults
Relay zone
Cross-faults
iii) Rotated block between cross-faults
140
260
Dip direction (°)
Corrugations continue across cross-fault
Rotation of the fault plane either side of cross-faults
c) Mapped corrugations
i) Corrugations along the splay fault
ii
i
ii) Rotation of corrugations across the cross-fault zone
0
5
10 m
170
210
Dip direction (°)
0
25
50 m

302

Figure 5: Fault plane geometry and corrugation trends for the Maghlaq Fault. a) Dip-direction map highlighting the rotation of the fault plane either side of major cross-faults and the presence of corrugations with insets i-iii showing detailed sections. b) Along-strike variation in dip-direction along the profile A-A', highlighting the changes in dip-direction used to map out corrugations and abrupt changes used to identify cross-faults. c) Map showing the trend of mapped corrugations (used to infer slip vectors) across the Maghlaq Fault. Black arrows indicate the average corrugation trend. Close up sections are highlighted to show i) how corrugation trend varies across the splay fault and ii) how corrugation trends are rotated by cross-faults. Note how fault plane geometry varies along the length of the studied section and that fault geometry and corrugation trend rotates close to, or between closely spaced, cross faults.

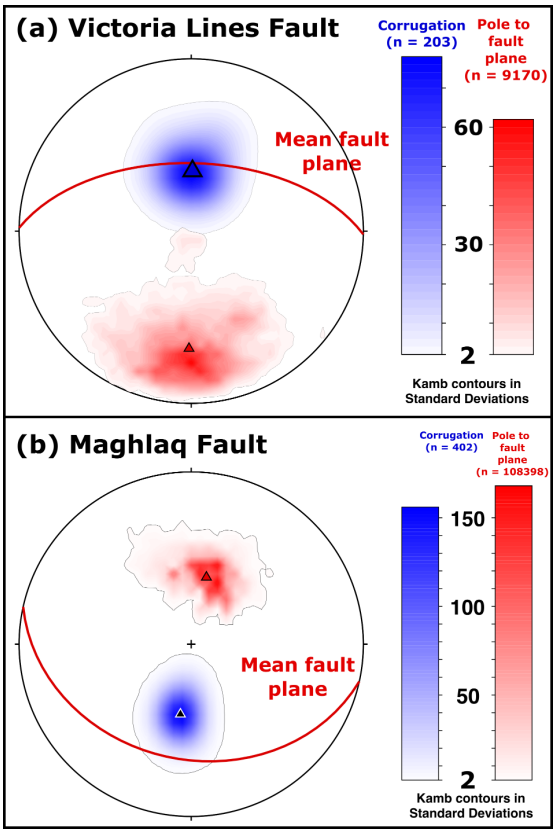

Figure 6: Stereographic projections of the (a) Victoria Lines and (b) Maghlaq faults showing the poles to the fault plane (red) and trend and plunge of mapped corrugations (blue). Triangles show the mean values of orientations of pole to the fault plane and of corrugations. Note the high dispersion in both fault plane geometry and corrugation trend, in part caused by the presence of cross faults that rotate the fault plane.

Along-strike variations in fault plane geometry are observed at multiple scale for both the Victoria Lines and Maghlaq faults (Figs. 4-6). The Victoria Lines Fault dips to the north, with a mean orientation of 001˚/58˚ (dip direction/dip), though dip and dip direction shows high variability as shown by the contours in Fig. 6a. The Maghlaq Fault dips to the south-southwest, with a mean orientation of 193˚/56˚, and exhibits similar dispersion in fault plane orientation as the Victoria Lines Fault (Fig 6b). Additionally, a splay fault with an average orientation of (160˚/67˚) was identified to the west of the study area (Fig 5a). Spatial analysis of dip-direction variations (Fig 4a,b, 5a) reveals that small-scale fault plane geometry changes occur at the meter to decimeter scale, while larger variations appear either as step changes or over short distances of <10 m (Fig 4b, 5a). Along-strike transects across these small-scale variations (e.g., Fig 4b) show a sigmoidal pattern in dip direction, with a change of dip direction of between 20˚ and 30˚ occurring over along-strike distances of between 5 to 20 m. These observations combined with the down-dip elongation of these features (Fig 5ai) has led to these being interpreted as corrugations.

Where abrupt changes in fault plane geometry occur, such as at ~245 m in Fig 4b and in the center of the Maghlaq Fault (Fig 5a), the change in dip direction frequently exceeds 20˚ and, in some locations, exceeds 45˚ over a distance of up to 15 m. These abrupt changes have been

interpreted as faults that intersect the main fault surface, hereafter termed cross-faults, which offset the fault scarp. Cross-fault mapping was conducted using dip-direction and dip-attribute maps, identifying 57 cross-faults on the Victoria Lines Fault and 535 on the Maghlaq Fault. The overall patterns and parameters of cross-faults are further explored in section 3.2.

Visual mapping of corrugations enabled abundant corrugations to be identified across the Victoria Lines (n = 203) and Maghlaq (n = 402) fault scarps (Fig 4c, 5b). The average corrugation orientations (61˚ -> 001˚and 56˚-> 189˚ respectively) indicate that both faults display normal slip vectors (Fig. 4). However, similar to the fault plane geometry, corrugation trends show high dispersion, ranging from 327˚ to 030˚ for the Victoria Lines Fault and 280˚ to 135˚ for the Maghlaq Fault (Fig 6). Spatial variations in corrugation trend reveal both similarities and differences between the two fault scarps. For both faults, corrugations either side of major cross-faults show a degree of rotation (Fig 4ci, 5bii). For the Victoria Lines Fault, corrugations exhibit 'convergent slip vectors' (cf. Roberts et al., 1996), with oblique corrugations towards the eastern and western edges of the study area (arrows in Fig 4c). This suggests that the Fomm Ir-RiH segment of the Victoria Lines Fault is behaving as an isolated fault, with its tips located near the study area's boundary. Conversly, the Maghlaq Fault shows no systematic changes in corrugation trend, other than in the vicinity of the splay fault, suggesting the study area is located in the center of a larger fault segment.

3.2 Cross-faults properties

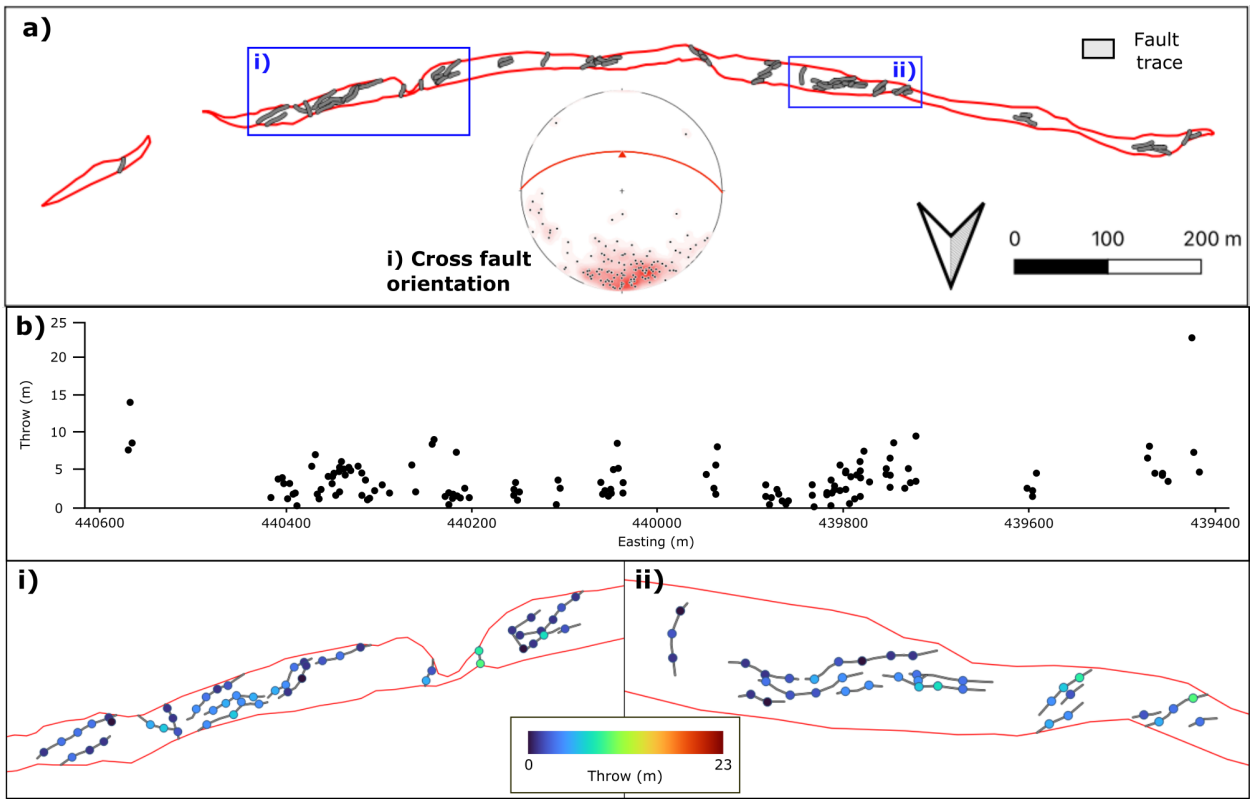

355

356 ***Figure 7: Cross-fault properties for the Victoria Lines Fault. a) Location of mapped cross-faults***
357 ***across the Victoria Lines Fault with an inset (i) highlighting their orientation. b) Along-strike***
358 ***distribution of cross-fault throw. How the throw distribution relates to the mapped cross-fault***
359 ***networks are shown in sub-panels bi and bii.***

360 Cross-faults mapped using the dip- and dip-direction attribute maps reveal similarities and
361 differences between the Victoria Lines and Maghlaq Faults (Fig 7, 8). Across the Victoria Lines
362 Fault, cross-faults are observed across the whole study area, forming fault zones where the cross-
363 fault perpendicular extent of mapped cross-faults ranges from 2 to 15 m (Fig 7a). Within these
364 zones, faults that intersect the main fault plane at high angles tend to exhibit slightly greater
365 throw than faults that intersect at a low angle (Figs 7b). This distribution pattern contrasts with
366 that observed along the Maghlaq Fault, where cross-fault distribution varies across the study

area (Fig 8). Fewer cross-faults were mapped in the western portion of the Maghlaq Fault, and the throw along these structures is typically below 2 m (Fig 8b). In contrast, the eastern portion of the Maghlaq Fault contains a larger number of small-offset cross-faults, leading to an overall increase in the rugosity of the main fault plane (Fig 5a, 8). The central portion of the Maghlaq Fault is characterized by high (up to 6 m) offset cross-fault zones composed of tens of individual cross-faults, which are separated by portions of the study area where less cross-faults are observed (Fig 8b). Cross-fault zones, where total throw across mapped strands exceeds 10 m, strongly influence fault plane geometry. These zones contribute to localized clockwise, or anticlockwise rotation of the fault plane, development of relay zones, and the formation of kinematically linked fault systems that span tens of meters perpendicular to cross-fault strike (Fig 8bi, bii). Both the Maghlaq and Victoria Lines Faullts show similar cross-fault patterns; however, the Maghlaq Fault exhibits a higher frequency of small-throw faults compared to the Victoria Lines Fault.

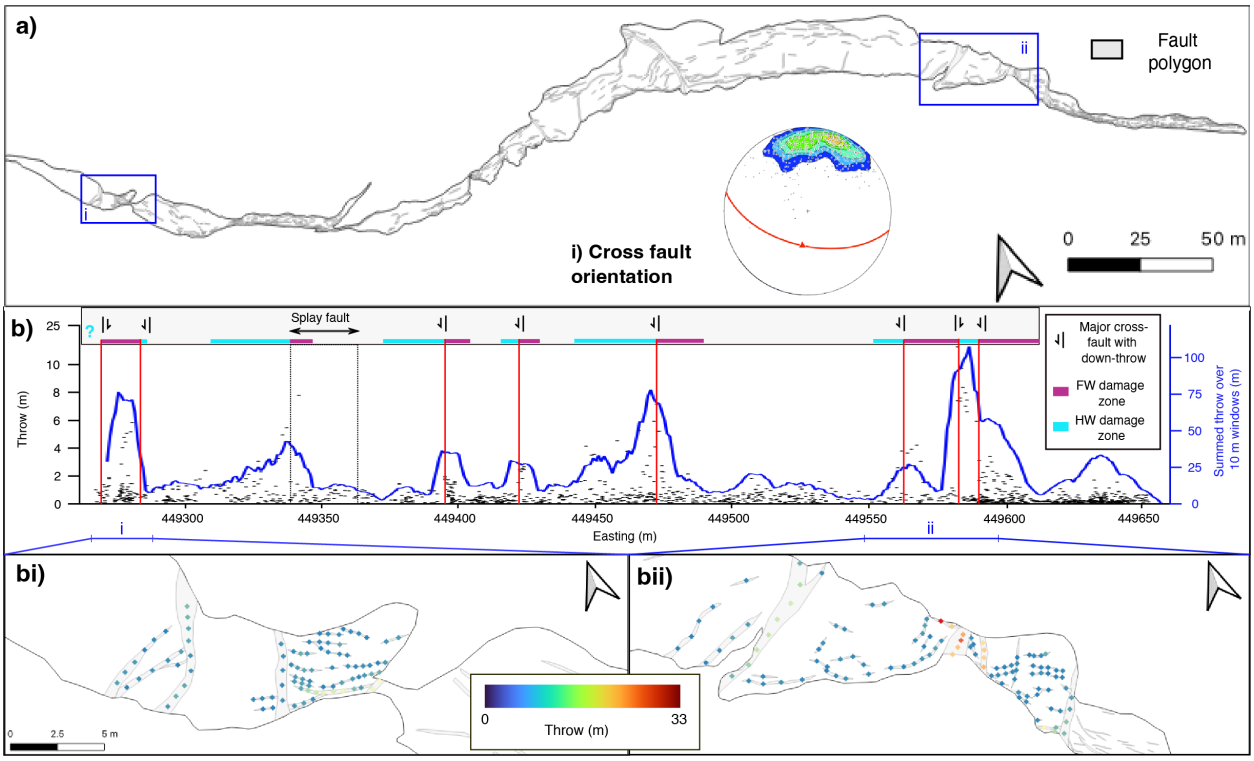

Figure 8) ***Cross-fault properties for the Maghlaq Fault. a) Location of mapped cross-faults across the Maghlaq Fault with an inset ai highlighting the orientation of all mapped cross-faults. b) Along-strike distribution of cross-fault throw. Note that because of the high number of mappable cross-faults, a rolling summed throw over 10 m windows was also undertaken, enabling the identification of cross-fault damage zones. How the throw distribution relates to the mapped fault networks are shown in sub-panels bi and bii.***

Cross-faults along both faults display a variability in extracted cross-fault properties (**Fig 7, 8**). Cross-faults display a broad range of orientations, with distinct average trends and downthrow directions between study areas. Cross-faults across the Victoria Lines Fault have an average trend of 073˚ and most faults downthrowing to the north compared to 104˚ with downthrow directions

to the south to southwest for the Maghlaq Fault (**Fig 7a, b**). The map-view length and throw of cross-fault also show considerable differences between the two faults, with cross-faults across the Maghlaq Fault typically being shorter and having a greater range, and lower average, throw (**Fig 8c, d**). This difference results in a higher proportion of censored cross-faults along the Victoria Lines Fault (37%) compared to the Maghlaq Fault (18%). The differences in throw and length leads to higher throw-to-length ratios along the Maghlaq Fault relative to the Victoria Lines Fault.

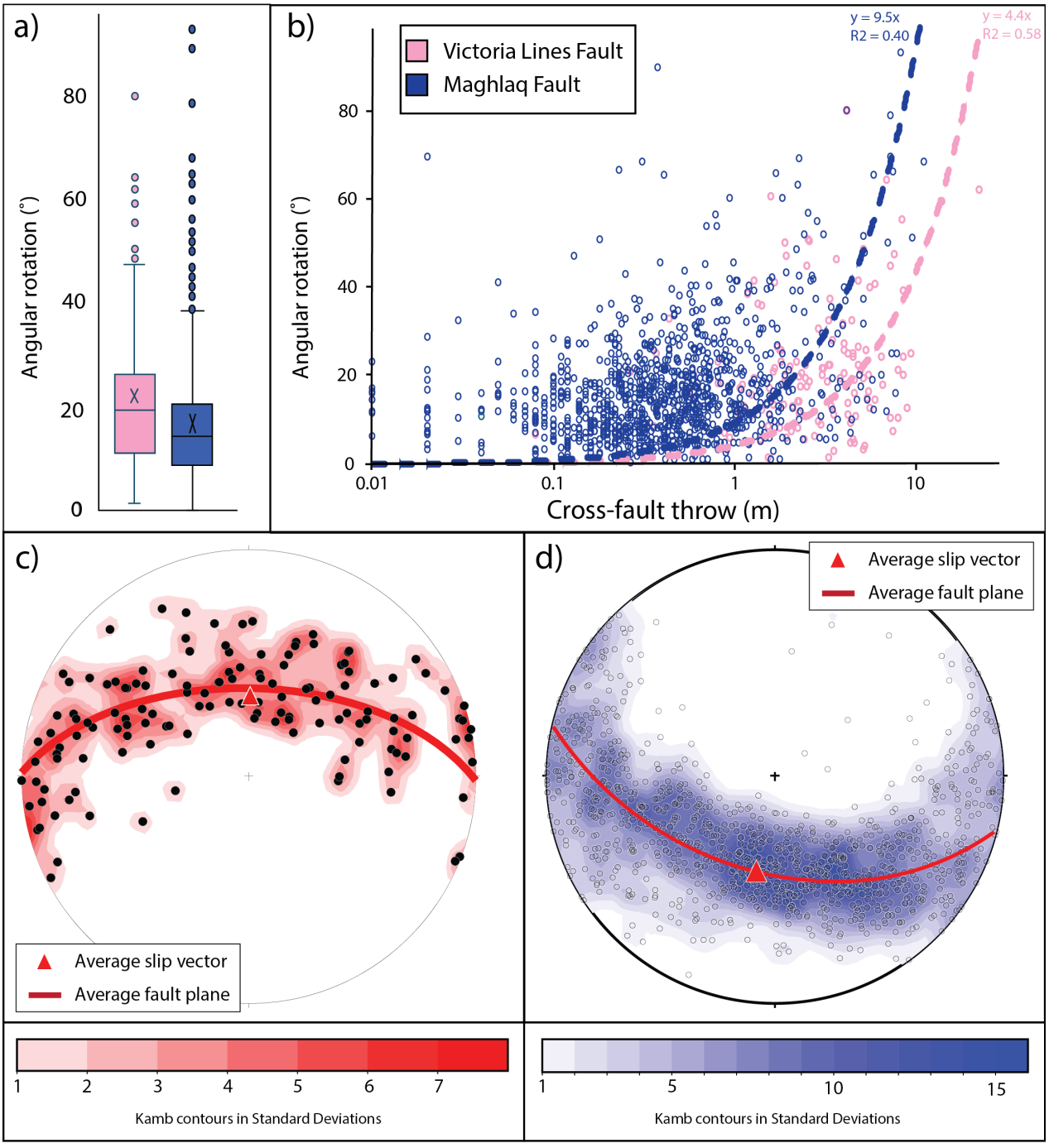

Figure 9: Angular rotation of main fault plane caused by cross-faults: a) Box and whisker plot of angular rotations caused by cross-faults for the Victoria Lines and Maghlaq faults. X refers to the mean angular rotation. b) Relationship between cross-fault throw and magnitude of

angular rotation. Stereographic projections of the rotation poles for the c) Victoria Lines Fault and d) Maghlaq Faults.

Either side of cross-faults, measurable rotations of the main fault plane orientation are observed (Fig 4a, 5a, 9). These rotations were quantified by analyzing cross-fault transects and extracting fault plane orientations from the footwall, hanging wall and fault plane of cross-faults (Fig 3b). Angular rotations of up to 55˚ were recorded, with median values of 20° and 17° for the Victoria Lines and Maghlaq Faults, respectively (Fig. 9a). A weak positive correlation is observed between angular rotation and throw (Fig 9b), though the relationship varies across different segments of the fault (Figs. 4a, 5a). Rotation axes cluster around the mean fault plane orientation, with a wide spread occurring along this plane (Fig 9 c, d). There is a slight concentration of rotation planes close to the mean slip-vectors of both faults, but no clear patterns can be observed from this data. Fault plane rotation is further evidenced by changes in corrugation trends near major cross-faults. Across both faults, corrugation orientations are rotated either side of cross-faults (Figs. 4c, 5b). For example, in the central portion of the Victoria Lines Fault, a southeast-trending cross-fault induces an 18° rotation in corrugations, shifting their orientation from 62° → 344° to 57° → 017° (Fig. 4ci). Similarly, along the Maghlaq Fault, multiple locations exhibit block rotation of corrugations adjacent to cross-fault zones that exceed 10 m throw (Figs. 5dii). The magnitude of these corrugation rotations is comparable to the angular rotation observed in overall fault plane geometry (Fig. 4b, 5a). This pattern suggests that fault corrugations developed prior to cross-fault formation in response to the early stages of normal faulting. Due to the resolution of the imagery, it is not possible to test whether any other forms of kinematic marker (e.g., striations) are rotated by cross-faults.

3.3 On-fault fractures on the Maghlaq Fault

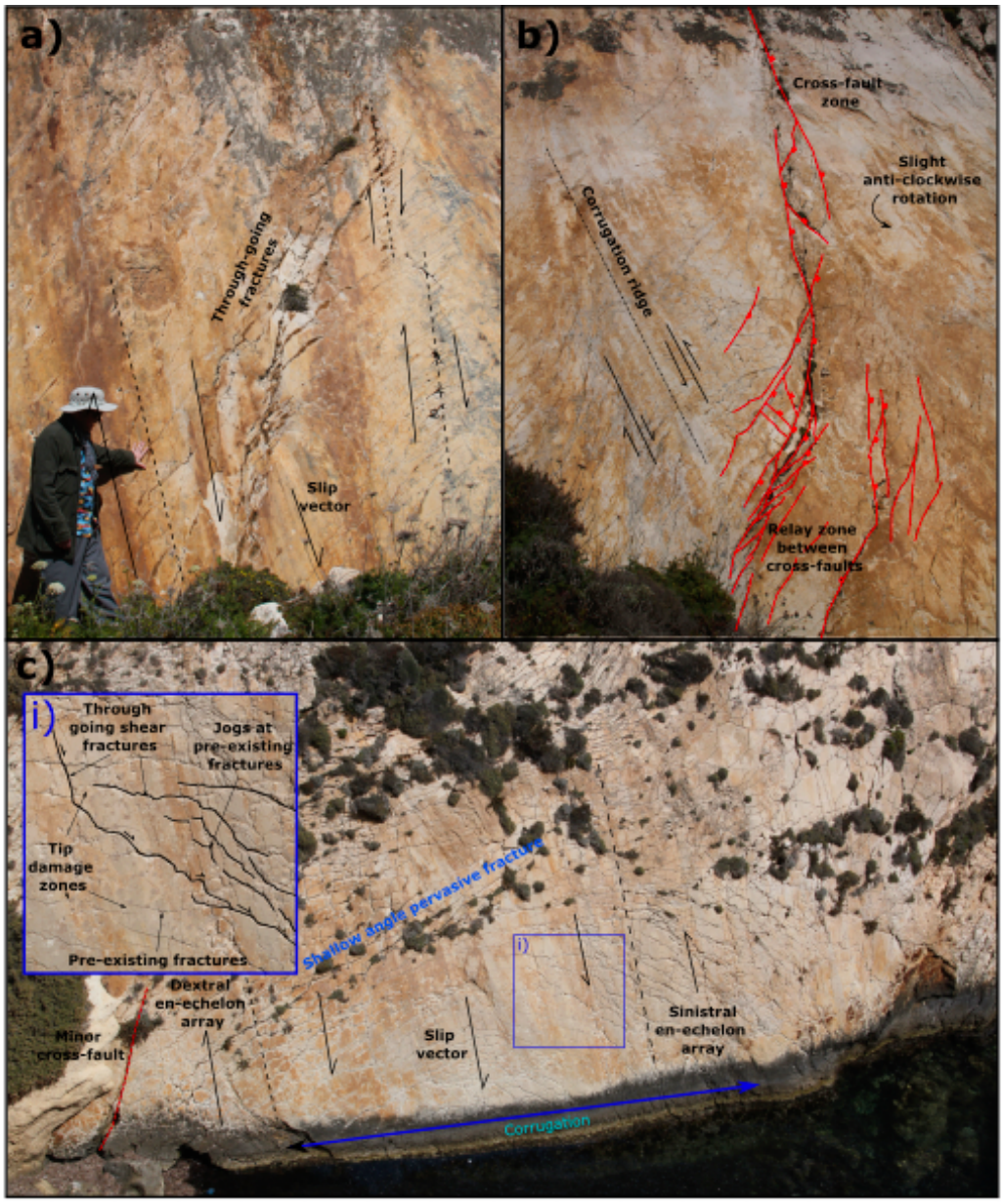

Figure 10: Field photographs of on-fault fractures on the Maghlaq Fault showing a) through-going fractures and en-echelon arrays cutting across a minor corrugation; b) minor cross-fault zone showing how cross-faults interact with on-fault fractures; c) en-echelon arrays either side of a corrugation, with the dashed lines representing the corrugation ridges where the arrays

nucleate, with the corrugation trough occurring where slip-vector is marked. The inset (i) highlights how through going shear fractures interact with pre-existing on-fault fractures.

The well-exposed slip surface of the Maghlaq Fault exhibits an extensive fracture network that provides an exceptional opportunity to analyze fracture patterns and along-strike trends in on-fault fracture properties, and infer their development (Fig 10-12). On-fault fractures occur as either opening-mode fractures with no disernable offset, or shear fractures with cm offsets, with no evidence of mineralization on either fracture type (Fig 10). Fractures are commonly en echelon, with the trend of the arrays aligned within 20˚ of the observed slip vector, as defined by striations and corrugations on the fault surface (Fig 10). These arrays can be either sinistral or dextral, with the sense of shear reversing across corrugation ridges and troughs (Figs 10b, c). Arrays occur either as isolated features, where fractures of similar length terminate at i-nodes (Fig 10a), or as linked structures that form larger connected fractures (i.e., through-going fractures), with trace lengths ranging from tens of centimeters to over a meter (Fig 10c). Where through-going fractures (i.e., fractures that cut across and utilize pre-existing fractures in the network) develop, tip-damage zones (cf. Kim et al., 2004) occur between fracture tips, and jogs are observed where a through-going fracture steps between previously isolated fractures (Fig 10ci). This suggests that there is a degree of shear across these fractures as strain becomes progressively localized onto larger fractures, which evolve into faults, while smaller en-echelon fractures are gradually abandoned as the network evolves (Figs. 10a, 10ci, e.g., Cowie, 1998).

In some areas, through-going fractures exhibit cm-scale offsets (Fig 10ci), and in localized zones, these features evolved into the aforementioned cross-faults (Fig 10b). This likely occured through

453 the progressive linkage of shear fractures, such as those in Figure 10a. These zones can extend
454 several meters across the fault scarp, creating highly connected networks that displace the fault
455 plane (Fig 10b). More developed cross-fault zones display centimeter- to decimeter-scale out-of-
456 plane offsets, resulting in a non-planar fault surface with a well-developed damage zone and
457 relay ramps between segments (Fig 10b). The throw observed across a single cross-fault mapped
458 using the dip- and dip-direction maps therefore probably represents throw accommodated by
459 several smaller structures and localized fault-plane rotation. These structures, as well as the
460 larger-scale cross-fault zones across the Victoria Lines and Maghlaq fault scarps (Fig 6), indicate
461 a systematic progression of deformation from isolated en-echelon fractures to cross-faults.
462
463 Systematic mapping of 27,459 on-fault fractures on the Maghlaq Fault at a scale of 1:50 highlights
464 the spatial variations in fracture intensity, connectivity, and trace length (Fig 11). Fracture
465 intensity ranges from 0.04 f/m to 7.52 f/m (mean = 2.55 f/m) while fracture lengths vary between
466 0.05 m and 18.44 m (average = 0.94 m). Smaller fractures typically form arrays, whereas larger
467 fractures exhibit greater connectivity and are more commonly located near cross-faults (Figs
468 10c,11c, d). The highest fracture intensities coincide with areas containing a greater proportion
469 of through-going fractures (i.e., fractures that utilize pre-existing fractures in the network) and
470 cross-faults (Fig 11a). Network connectivity is also high, with a percentage of connected branches
471 (Pc) of 85%, with the majority of nodes classified as Y-nodes (50.3%), followed by I-nodes (34.9%)
472 and X-nodes (14.7%) (Fig. 11d). Connectivity, however, displays significant variations across the
473 study area (Fig 11d). In general, fracture intensity and connectivity are higher towards the eastern
474 portion of the study area, where small offset cross-faults are more frequent, while the western

475 portion exhibits lower intensities, except in the vicinity of large offset cross-faults. These trends
476 indicate a strong spatial correlation between fracture network properties and cross-faults.
477

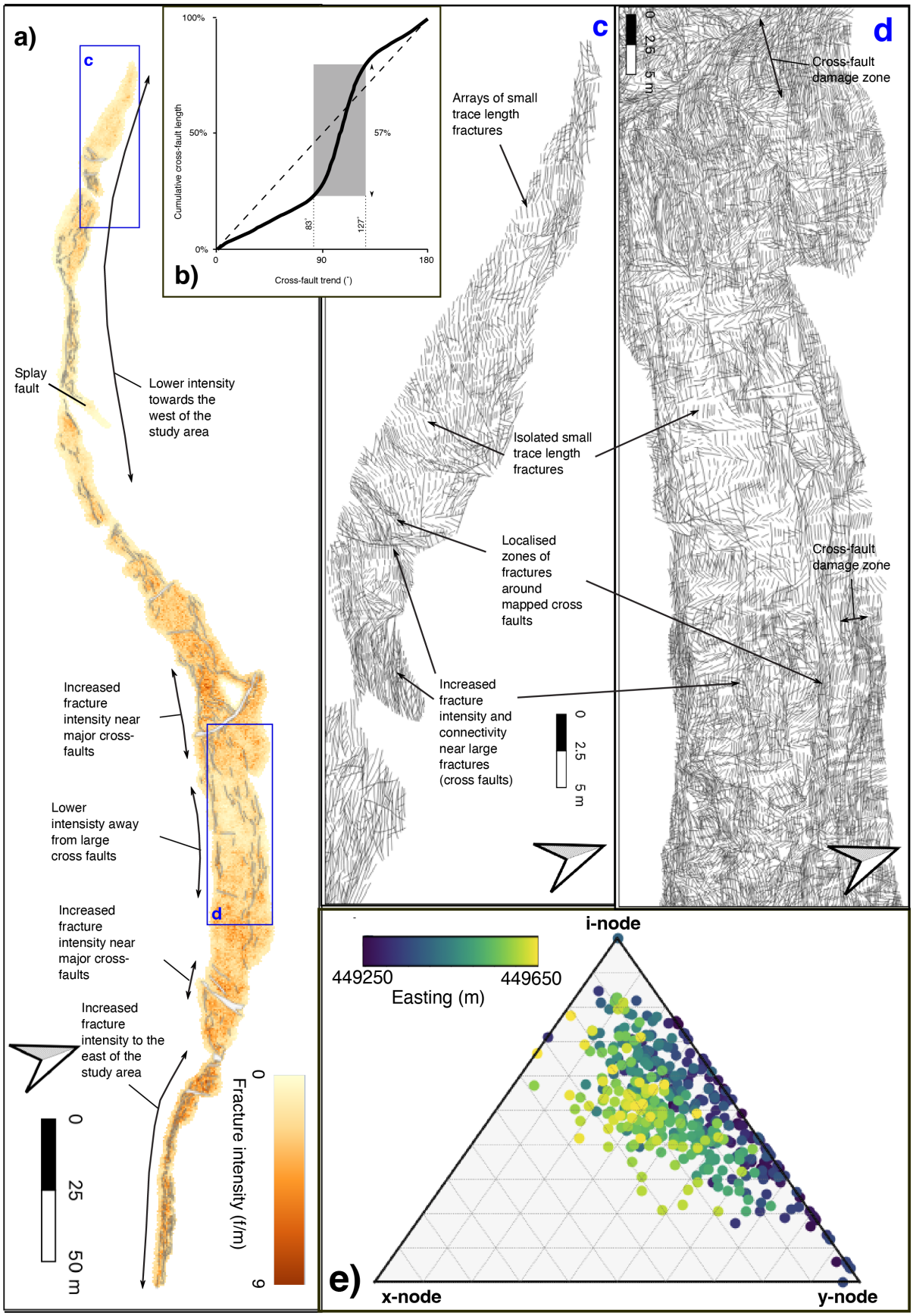
a)
c
d
Splay fault
Lower intensity towards the west of the study area
Increased fracture intensity near major cross-faults
Lower intensisty away from large cross faults
Increased fracture intensity near major cross-faults
Increased fracture intensity to the east of the study area
0
25
50 m
Fracture intensity (f/m)
0
9
b)
100%
50%
0%
Cumulative cross-fault length
57%
83°
127°
0
90
180
Cross-fault trend (°)
c
Arrays of small trace length fractures
Isolated small trace length fractures
Localised zones of fractures around mapped cross faults
Increased fracture intensity and connectivity near large fractures (cross faults)
0
2.5
5 m
d
0
2.5
5 m
Cross-fault damage zone
Cross-fault damage zone
e)
i-node
449250
449650
Easting (m)
x-node
y-node

478

Figure 11: Fracture properties across the Maghlaq Fault. a) Fracture intensity (P10) map across the MF. b) Trend of all mapped on-fault fractures. c-d) Insets of the digitized network highlighting key features discussed in the main text. e) Node triangle showing the distribution of node classifications across the study area.

On-fault fracture properties display both gradual variations over distances of tens of meters and abrupt step-changes at cross-faults with > 10 m cumulative throw (**Fig 12**). Gradual changes correspond to changes in fault plane geometry at corrugations (**Fig 12**). This relationship is observed at feature 'CA' in **Figure 12**, where a corrugation with a 30˚ change in dip direction over a 40 m along-strike distance coincides with a localized increase with fault dip. On-fault fractures within the corrugation show a change in orientation from ESE to SE before returning to ESE, fracture intensity decreases from 2 f/m to 1 f/m, while network connectivity increases at the boundary of the corrugation, before decreasing in the trough (**Fig 12**). Similar trends are observed across the study area, and in the detailed field photographs (**Fig 10c**). Additionally, the effect of fault plane geometry on fracture network properties is evidenced where the splay fault intersects the fault scarp (Fig 5a, 12a), where a bimodal distribution of on-fault fracture orientation (Fig.12d), and an increase in fracture intensity and connectivity (Fig. 12e-f), is observed as the fault segments link (**Fig 12**). Overall, corrugation ridges appear to cause an increase in fracture intensity and connectivity when compared to corrugation troughs, and the orientation of on-fault fractures is related to the orientation of the fault plane (**Fig 10c, 12a-d**).

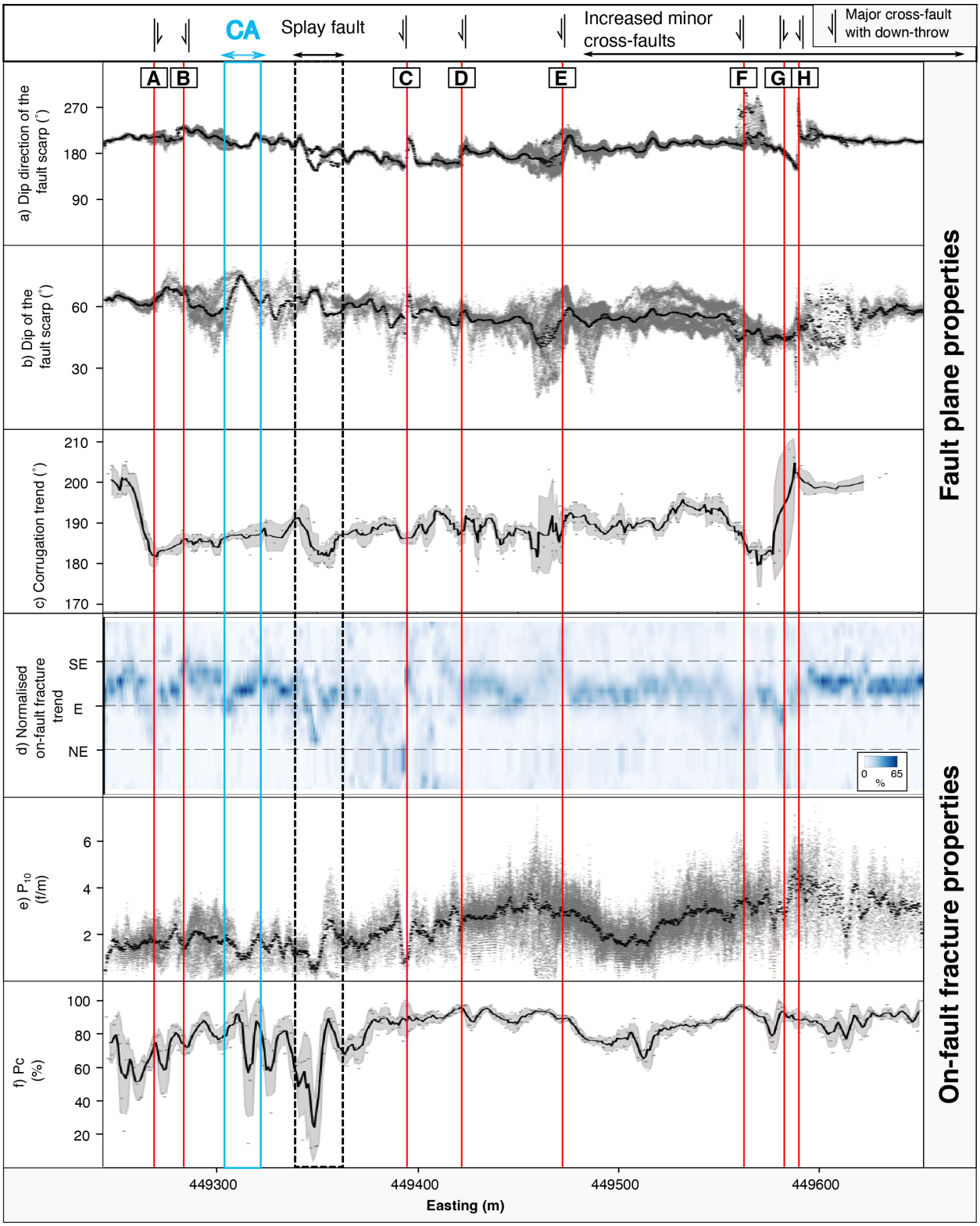
CA
Splay fault
Increased minor cross-faults
Major cross-fault with down-throw
A
B
C
D
E
F
G
H
a) Dip direction of the fault scarp (°)
270
180
90
b) Dip of the fault scarp (°)
60
30
c) Corrugation trend (°)
210
200
190
180
170
Fault plane properties
d) Normalised on-fault fracture trend
SE
E
NE
0
65
%
e) P10 (f/m)
6
4
2
f) Pc (%)
100
80
60
40
20
On-fault fracture properties
449300
449400
449500
449600
Easting (m)

Figure 12: Along-strike trends in fault plane and on fault fracture properties across the Maghlaq Fault, with the location of major cross-faults indicated with red vertical lines. a) Dip-direction of the Maghlaq Fault. b) Dip- of the Maghlaq Fault. For panels (a) and (b), the grey dots show individual sampled values, whilst the black line shows the average for a given easting value. c) Corrugation trend of mapped corrugations, showing all mapped corrugations (grey dots), rolling average (n = 5), and standard deviation (grey shade). d) Heat map showing the normalized on-fault fracture trend by 5 m along-strike bins. e) Fracture intensity (P10), showing each datapoint (grey) and a 5 m wide rolling average (black). f) Percentage of connected nodes showing all sample circles (grey dots), a rolling average (n = 5), and standard deviation (grey shade).

Properties of on-fault fractures are strongly influenced by the presence of cross-faults. Mapping of cross-faults identified a series of cross-fault zones (A-H), which correspond to changes in on-fault fracture properties (Figs. 6d-f, 12). Step-changes in fracture trend, intensity, and connectivity are frequently observed at these locations (Fig. 12d-f). For example, on-fault fracture trend changes from 116˚ in the footwall of cross-fault zone H to 096˚ in the footwall of cross-fault zone G (Fig. 12d). This aligns closely with the 23˚ rotation in fault-plane orientation across the same faults (Fig. 12a), suggesting that some on-fault fractures must predate cross-faults and have been block-rotated during faulting. Compared to on-fault fracture orientation, fracture intensity (Fig. 12e) and connectivity (Fig. 12f) exhibit more variable responses to cross-faults. In some cases, step changes occur immediately adjacent to cross-fault zones (e.g., cross-fault zones G, H), whereas in others, a more gradual increase is observed approaching the fault zones (cross-fault zones A, D, E). A decrease in fracture intensity and connectivity is recorded

521 across cross-fault zones B and C, but this appears to be caused by preferential erosion of the fault
522 plane at these locations, which reduces the image resolution close to those cross-fault zones.
523 Fracture intensity and connectivity are low in the western portion of the study area, where cross-
524 fault density and throw are relatively low (Fig11e-f). In the eastern portion, where small offset
525 cross-faults are abundant, fracture intensity and connectivity are high and show a greater
526 variability compared to elsewhere in the study area (Fig 11e-f). These observations suggest that
527 while cross-faults post-date some on-fault fractures, as evidenced by the rotation of the fracture
528 orientations, fractures continued to form and the fracture network developed after the cross-
529 faults developed, as shown by cross-faults modifying intensity (Fig 12e) and connectivity (Fig 12f)
530 patterns. This implies a progressive deformation history for the Maghlaq Fault Scarp, which is
531 explored in the discussion.

4 Discussion

4.1 Evolution of brittle deformation across the Victoria Lines and Maghlaq faults

We deduced a four-stage structural evolution of the studied fault scarps from the detailed analysis of fault plane geometry, on-fault fracture mapping, and the identification of cross-faults

(Fig 13). The proposed structural evolution serves a as basis for the discussion on the spatial and temporal evolution of energy dissipation through brittle deformation in Section 4.2

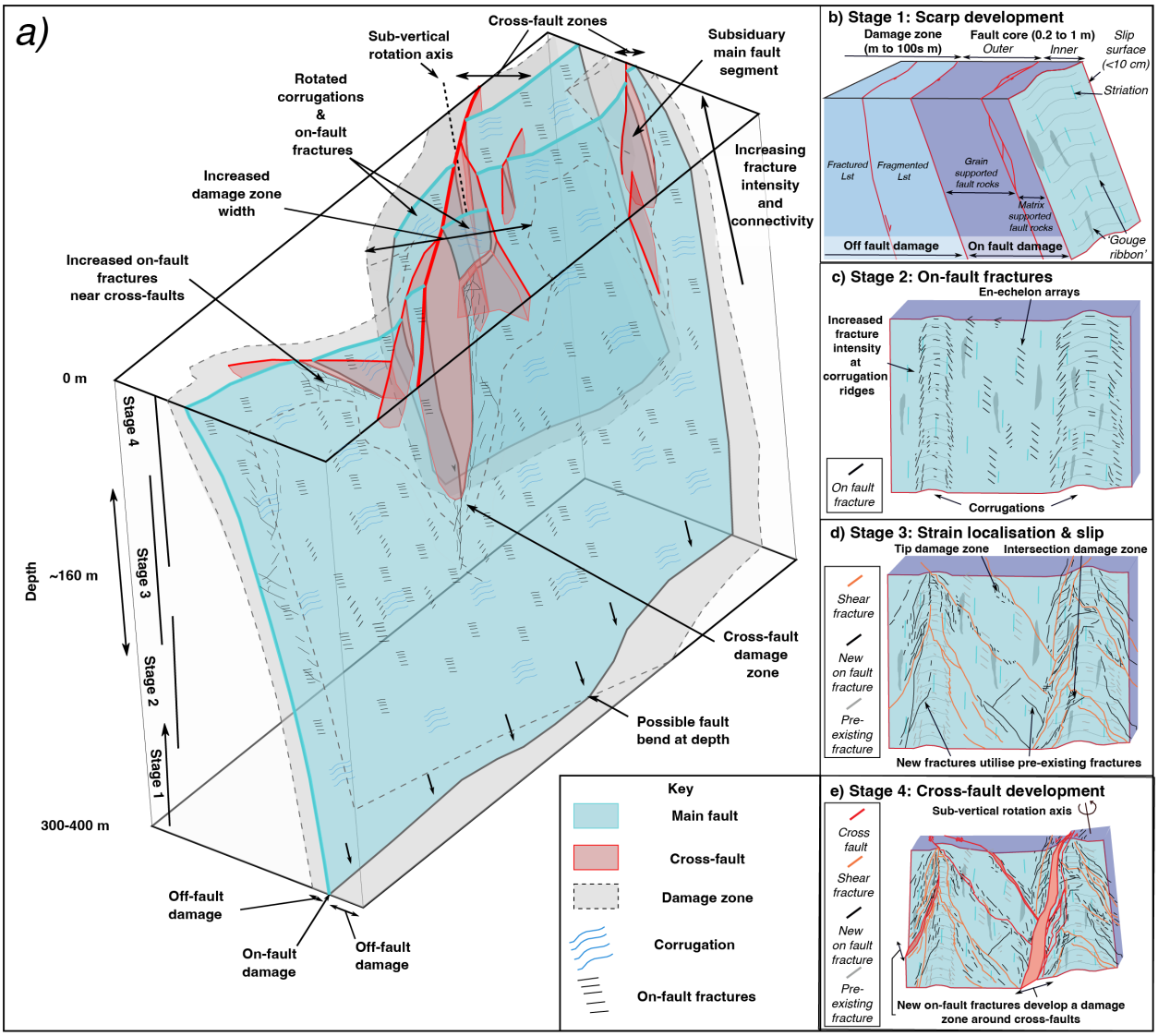

Fig 13: Conceptual model outlining the key stages of brittle deformation: a) conceptual model of deformation at depth based on the observed cross-cutting relationships; b) conceptual model of limestone fault scarps after (Ferraro et al., 2018); c-e) conceptual evolutionary model

542 **highlighting the progressive on-fault deformation of non-planar fault scarps during footwall**
543 **uplift, see text for discussion.**

544 **Stage 1: Initial fault scarp development and corrugation formation (Fig 13b).** Faulting
545 initiated on the Victoria Lines and Maghlaq faults during the late syn-rift phase (~7 to 5 Ma), with
546 the maximum burial of footwall sediments not exceeding 250 to 300 m (Bonson et al., 2007; Dart
547 et al., 1993; Martinelli et al., 2019; Villani et al., 2018). The Victoria Lines and Maghlaq faults have
548 well-developed bedrock fault scarps that preserve corrugations (Fig 5). As normal faults accrue
549 throw and deformation of the fault scarp, the footwall uplifts relative to the hanging wall
550 (Doutsos & Koukouvelas, 1998; Quye-Sawyer et al., 2021; Schlische & Anders, 1996; Stein et al.,
551 1988; Stein & Barrientos, 1985), with uplift to subsidence ratios for the Mediterranean commonly
552 1:1.6 to 1:2.3 (Doutsos & Koukouvelas, 1998; Quye-Sawyer et al., 2021; Stein et al., 1988).
553 Therefore, the fault scarp and footwall were progressively exhumed over time. Based on this
554 burial and tectonic history, fault scarp development and subsequent brittle deformation must
555 have occurred in the top 200 to 300 m of the crust.

556 Corrugation trends across the Victoria Lines Fault show convergent slip vectors, where
557 slip is nearly dip-slip in the faults center and becomes more oblique towards the tips (Fig 5). Such
558 patterns, recognized across many active normal faults (e.g., Jackson et al., 1982; Roberts 1996;
559 Roberts and Ganas, 2000; Roberts and Michetti, 2004; Michetti et al., 2000; Maerten, 2000), and
560 are used to distinguish kinematically isolated verses connected fault segments. Where not
561 influenced by cross-fault rotations, corrugation trends along the Maghlaq Fault remain close to
562 dip-parallel (i.e. , normal fault slip) with little to no evidence of convergence (Fig. 5b), implying

563 that the fault tips lie outside the study area. This aligns with Bonson et al. (2007), who interpret
564 the Maghlaq Fault as initially comprising WNW-ESE trending isolated segments that were later
565 linked by NE-SW trending branch faults, likely forming at a depth below 160 m. Corrugations on
566 the splay fault (Fig 5ai), and evidence of SSW-directed slip prior to cross-fault rotation, support a
567 protracted linkage history on the Maghlaq Fault. In contrast, corrugations across the Victoria
568 Lines Fault are consistent with the study area being an individual fault segment. This is supported
569 by throw distributions (fig 7b), which decrease eastward, and the segment tipping out onshore
570 (Fig 2b, c; Villani et al., 2018). Thus, although the faults share some features and both develop
571 cross-faults, the Maghlaq Fault has a more protracted linkage history, providing insights into the
572 role of this on subsequent brittle deformation.

573 **Stage 2: Early on-fault fracture formation (Fig 13c).** On-fault fractures across the Maghlaq
574 Fault cross-cut the fault scarp, so must post-date the formation of the fault scarp and
575 corrugations. Most small (<2 m) trace length on-fault fractures mapped across the Maghlaq Fault
576 have isolated nodes and form sinistral or dextral arrays, with the array trends close to the
577 observed corrugation trend (Fig 10, 11ai, aii). Abundant aligned en echelon fractures are
578 indicative of pure shear dominated transtension (Dewey et al., 1998; Fossen and Tickoff, 1998;
579 Sanderson and Marchini, 1984). In the case of the Maghlaq Fault, shear occurs down the
580 corrugation trend and a degree of extension occurs across the fault surface.

581 In addition to overall trends, changes in fracture orientation and array shear sense, coupled with
582 an increase in fracture intensity, are observed around geometrical complexities (**Fig 10c)** related
583 to corrugation ridges and troughs (Fig 12). Geometrical complexities are known to influence the

584 near-fault stress field (Chester and Chester, 2000) and the type and distribution of fault rocks
585 across the fault surface, and often refer to as “asperities” (Scholz, 2002; Chambon et al., 2006).
586 Large asperities, whether geometrical or rheological, commonly act as areas of increased stress
587 accumulation and causes earthquakes to nucleate at this location (Aki, 1984). Smaller
588 geometrical heterogeneities can directly influence the velocity and behavior of an earthquake
589 rupture, reducing an earthquakes rupture velocity and acting as a barrier to slip, limiting the size
590 and extent of ruptures (Li et al., 2023; Wesnousky, 2006; Zhang et al., 2023). This reduction in
591 rupture velocity can explain the local change in dominant array type across corrugation ridges
592 and troughs, whereby the bulk velocity decreases locally around the asperity relative to the
593 overall trends observed across the fault surface. Our observations suggest small geometrical
594 variations across the fault surface are sufficient to increase the degree of on-fault fracturing and
595 may locally perturb the velocity field across the fault surface during earthquakes.

596 **Stage 3: Strain localization and slip along on-fault fractures (Fig 13d).** Cross-cutting and abutting
597 relationships reveal that as a sub-section of the network grow, tip damage zones develop as on-
598 fault fractures from different en-echelon fractures interact (Fig 10ci). Tip damage zones (e.g., Kim
599 et al., 2004) suggest a minor amount of shear occurs along the fractures. These fractures form a
600 throughgoing shear fracture that displays abundant jogs at the intersection with pre-existing
601 fractures (Fig 10ci). As fracture networks evolve, strain commonly becomes localized onto a
602 subset of fractures, preserving blocks of early fractures that no longer accrue strain surrounded
603 by larger fractures that do (Cowie, 1998; Cowie et al., 2005; Segall & Pollard, 1983). The
604 orientation and spacing of the pre-existing fractures within a network is known to strongly
605 influence the properties (e.g., length, connectivity, orientation) of subsequent fractures (e.g.,

(Cruikshank et al., 1991; Peacock et al., 2018, 2023; Peacock & Sanderson, 2018). Across the Maghlaq Fault, longer (>2 m) through-going fractures show this clearly, with rapid changes in orientation present where through-going fractures intersect with isolated en-echelon fractures (Fig 10a, b), causing localized (up to 2 m wide) increases in the length, connectivity, and intensity of fractures across the Maghlaq Fault Scarp (Fig 11a, ai, aii). Similarly to isolated on-fault fractures, the location of these localized zones of increased fracturing correlate with small wavelength changes in fault plane geometry (Fig 12), suggesting geometrical variations also control the location of strain localization across the fault scarp. Additionally, as fractures display evidence of progressive growth over multiple earthquake cycles, it suggests geometrical variations continue to act as asperities as the footwall is uplifted during shallow earthquake slip.

Stage 4: Cross-fault development and rotation of the fault scarp (Fig 13e). Numerous cross-faults are observed across both studied fault scarps, and post-date and rotate the fault planes and corrugations (Fig, 7, 8), as well as a subset of the on-fault fractures on the Maghlaq Fault (Figs 12). Cross-faults are typically longer across the Victoria Lines Fault and have greater throw than those across the Maghlaq Fault (Figure 7). This may be partly caused by the difference in resolution between the DEMs of the Victoria Lines (pixel size = 0.13 m) and Maghlaq (pixel size = 0.06 m), leading to the smallest cross-faults across the Victoria Lines Fault to be below the resolution of the dataset. Despite this, cross-faults across both datasets show high throw values

for their respective lengths and are overdisplaced when compared to global datasets of normal faults (e.g., (Lathrop et al., 2022).

Suggestions for the formation of cross-faults include: i) strain compatibility associated with relay ramp development (Walsh and Watterson, 1991; Long and Imber, 2021); ii) the presence of weak fault rock along non-oriented fault segments (ref); iii) the presence of pre-existing faults and/or structural inheritance (Phillips et al., XXX; Pizzi and Galadini, 2009). Options (i) and (ii) require the presence of faults that are separate, and at a high angle to, the main fault. Cross-faults in our dataset typically occur within 25˚ of the main faults strike and show a progressive evolution after the main fault slipped in a different direction (Fig 4, 5), therefore this observation implies (i) and (iii) are unlikely. The only remaining viable explanation, where cross-faults develop because of strain incompatability during relay ramp development, could match previous models of fault growth for the Maghlaq Fault. Using detailed fault zone mapping, Bonson et al. (2007) suggest the Maghlaq Fault displays evidence of progressive smoothing and linkage during the development of a breached relay ramp. The linkage of fault strands, as evidenced by the presence of the splay fault (Fig. 5), may contribute to the increased cross-fault intensity across the Maghlaq Fault compared to the Victoria Lines Fault. Contrary to the findings of Bonson et al. (2007), however, we find that cross-faults act to rotate the fault scarp and therefore increase the rugosity of the overall slip surface. Additionally, the evidence of convergent slip vectors across the Victoria Lines Fault suggests that this fault slipped as an isolated segment (e.g., Roberts et al., 1996), but still displays similar cross-fault patterns and orientations to the Maghlaq Fault. Cross-faults rotating the fault plane and the elevated fracture intensity around cross-faults therefore indicate that cross-faults begin to form at geometrical

heterogeneities, and the presence of cross-faults across both studied faults, indicates that cross-faults likely form in response to stress rotations and irregular slip patterns that occur around geometrical heterogeneity during shallow earthquakes (e.g., Marshall and Morris, 2012; Resor and Meer, 2009).

4.2: The effect of brittle deformation on energy dissipation during shallow earthquakes

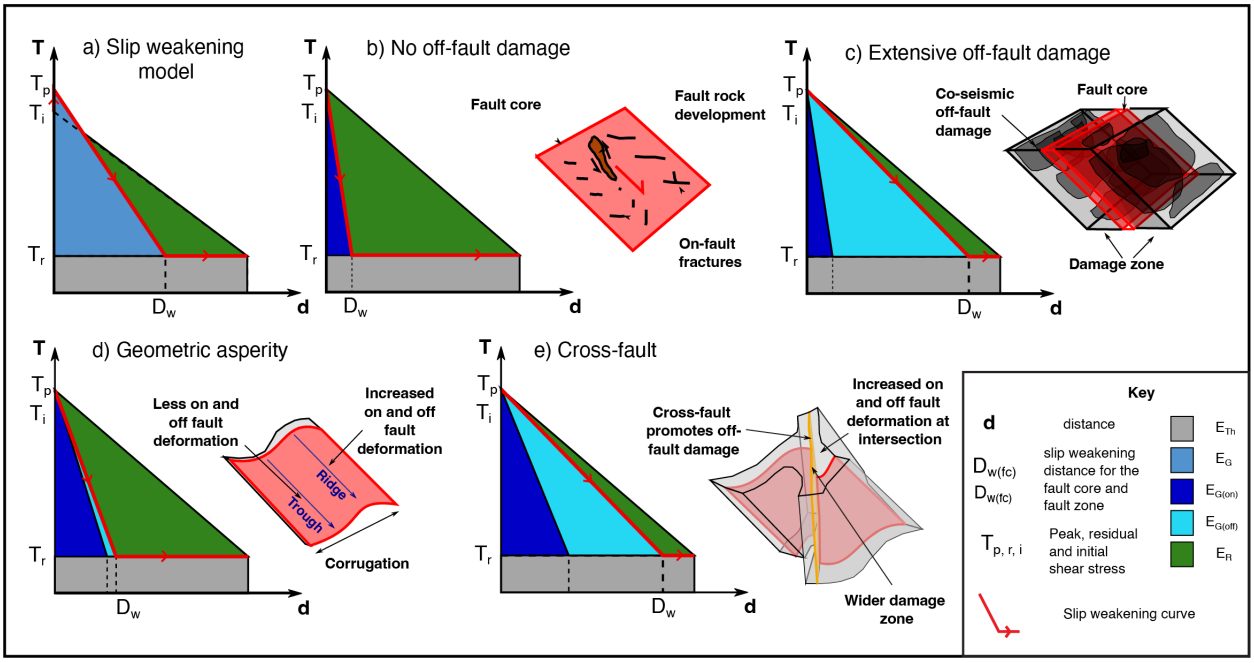

Figure 14: Graphical representations of the earthquake energy budget for a range of on-fault and near-fault deformation scenarios within a slip-weakening framework. Energy partitioning is illustrated for: a) a case in which breakdown work consists only of E_G required for rupture propagation (Kanamori and Rivera, 2006); b) deformation confined to the fault core, with on-fault damage and negligible off-fault damage, as often observed in high velocity rock mechanics experiments (De Paola et al., 2025); c) energy is dissipated within a faults damage zone (De Paola et al., 2025); d) minor geometrical asperities, where damage is constrained to the fault

659 **core prior to the development of throughgoing fractures and cross-faults; e) the vicinity of**
660 **cross-faults, where the magnitude of on- and near-fault damage increases. Where E_{Th} is the**
661 **energy dissipated within the fault zone through frictional heating, E_G is the fracture energy**
662 **required for rupture propagation, and can be split into energy dissipated within the fault core**
663 **(E_{Gon}) and energy dissipated within a faults damage zone (E_{Goff}), and E_R is the radiated energy**
664 **through seismic waves.**

665 Faults are heterogeneous, displaying geometrical, structural and lithological variations across the
666 fault surface that can directly affect earthquake rupture mechanics (e.g., Abercombie et al., 2006;
667 Faulkner et al., 2003; Mashoch et al., 2021; Coco et al., 2023; McKay et al., 2020). Our study
668 highlights that in addition to spatial heterogeneities, spatial-temporal variations occur in the type
669 and distribution of on-fault deformation, and therefore on-fault energy dissipation, in the top
670 few hundred meters of the crust across multiple earthquake cycles. The main components of an
671 earthquakes energy budget can be graphically represented on a slip-weakening curve (Fig 14),
672 whereby the total fracture energy (E_G) dissipated during earthquake rupture is equal to the work
673 done by the earthquake within the fault core (i.e., on-fault, **E_{Gon}**) and off-fault fracturing in the
674 surrounding damage zone (**E_{Goff}**). The remaining energy is radiated as seismic waves (**E_R**), or
675 through thermal heating (**E_H**) (Cocco et al., 2023; Kanamori & Rivera, 2006; Nielsen et al., 2016).

676 Our results show that on-fault damage varies spatially across the fault surface, as evidenced by
677 the range in observed fracture intensity (0.2 to >4 f/m, Fig. 12). The slip-weakening distance (Dw)
678 (i.e., the amount of slip required for the shear stress to decrease from the peak strength to the
679 residual dynamic strength) and total dissipated fracture energy (**E_G**) will also vary (**Fig 15ii**).

Fracture intensity decreases where the fault plane is relatively planar (e.g., between cross-faults E and F in Fig 12). This suggests low on-fault energy dissipation (Fig 1b), enabling an increase in radiated energy, surface ruptures, and surface shaking. In our data, fracture intensity was observed to increase around geometrical heterogeneities, in particular at the edge of asperities (e.g., ridges of corrugations), suggesting increased on-fault energy dissipation at these locations (Fig 9, 11). Additionally, the prevalence of fractures that are large enough to propagate away from the fault surface propably promote an increase in off-fault damage, although this was not possible to quantify with the available datasets. In this case, Dw will be greater than in the case of a planar fault surface, and a lower proportion of the energy will be radiated as seismic waves (Fig 15iv).

The structural model (Fig. 14) suggests that on-fault fractures progressively develop during upper few 100 metres of the crust during earthquake slip (Figure 12a), with the observed network providing a final snapshot of on-fault deformation across multiple seismic cycles. To gain a better understanding of the evolution of energy dissipation through time, and to gain insights into different energy sinks during shallow earthquake slip, findings need to be considered in relation to the presented structural model. Prior to fracture development (Stage 1), on-fault energy dissipation occurred through the development of fault rocks that form a corrugated fault core. Following this (Stage 2), during early fracture development, short trace length (<1 m) on-fault fractures formed as arrays with their orientation influenced by minor asperities on the fault surface. As these fractures are small, their contribution to the overall earthquake energy budget will be limited, providing a minor energy sink across the whole fault surface. As strain localized onto a sub-set of the fractures (Stage 3), the length of on-fault fractures increased, and new on-

fault fractures evolved as damage zones around the sub-set of fractures. This increase in fracture length will increase the amount of fracture energy dissipated within the fault core and immediate damage zone. Additionally, the energy sink caused by these fracture zones is localized at geometrical heterogeneities, such as corrugation ridges, increasing the likelihood that these features influenced earthquake rupture patterns. As cross-faults develop (Stage 4), aseismic slip will be be transferred from the main fault into the damage zone, increasing off-fault deformation (Fig 8, 11). Both these factors will increase the slip-weakening distance (Dw). Additionally, a portion of earthquake energy will contribute to the rotation of the main fault surface, which will

also alter the relative angle of the main fault relative to the slip-direction creating a geometrical barrier to further slip.

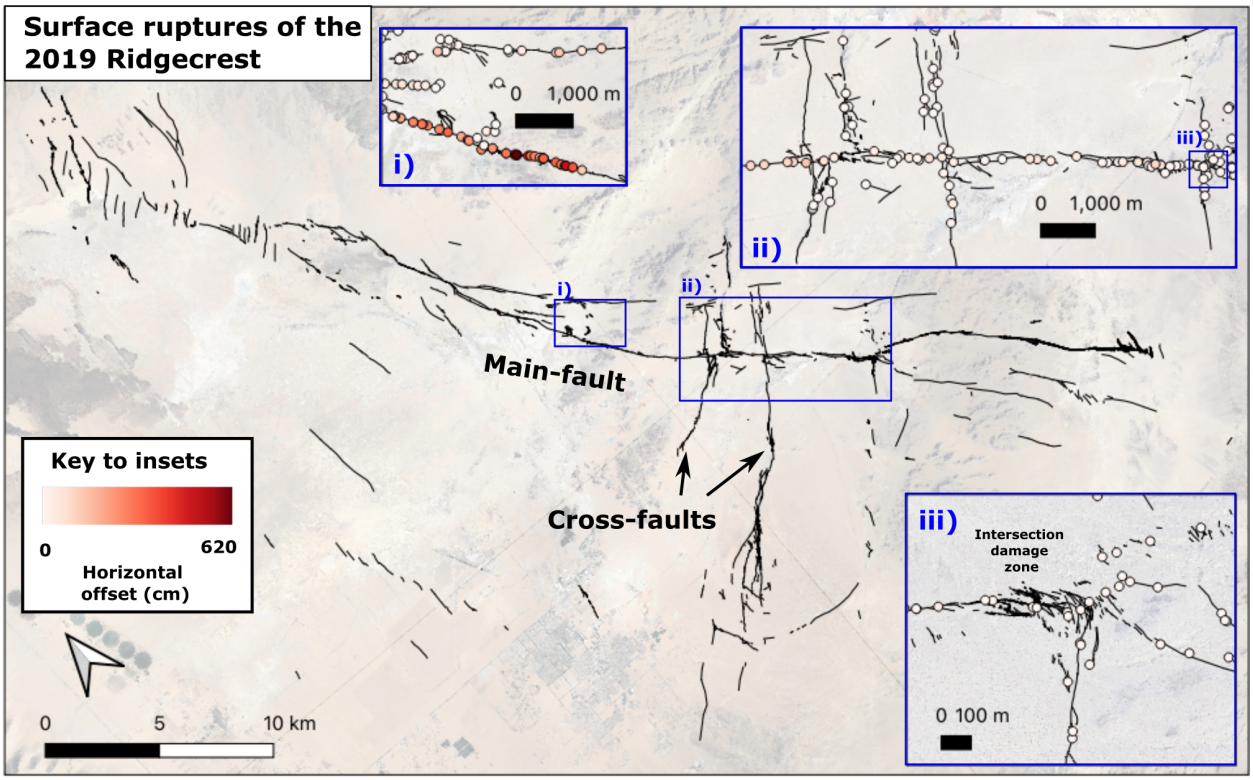

Figure 15: Surface rupture and horizontal offset of the Ridgecrest Earthquake. Insets highlight how the horizontal offset varies when segments of the fault with no surface ruptures (i) are compared to where cross-faults cross (ii) or intersect with (iii) the main fault strand.

Geometrical and/or rheological asperities strongly influence earthquake slip distributions (e.g., Lay et al., 1982). Faults are known to smooth as continued slip erodes asperities and slip becomes more energy efficient (Sagy & Brodsky, 2009; Kirkpatrick and Brodsky, 2014; Hayward et al., 2019; Imber et al., 2008). Most of these studies focus, however, on faults exhumed from depth and give little information about slip in the shallow surface. Our work has shown that on-fault fractures and cross-faults act to increase the geometrical complexity of the main fault through

722 time, with cross-faults being a type of geometric barrier, which can lead to slip being partitioned
723 into the damage zone. For example, during the 2019 Ridgecrest Earthquake (REF), cross-faults
724 caused an increase in the intensity of surface ruptures at the intersection of the cross-fault and
725 main fault (Fig 16ii, iii), as well as these areas having lower slip values compared to portions of
726 the fault where no cross-faults are present (Fig 16i). These are similar observations to the
727 patterns of cross faults observed in our study area, suggesting cross-faults, and their associated
728 damage zones, can have a significant impact on damaging surface rupturing earthquakes. Our
729 work highlights that the distribution of on-fault energy sinks in the near surface are spatially and
730 temporally variable, with cross-faults having a strong effect on the distribution of surface
731 ruptures and increased off-fault damage in the shallow sub-surface (Fig 15c). We therefore
732 suggest that the further study of on-fault fracture networks in natural and laboratory examples
733 can provide valuable insights into the shallow earthquake energy budget, how this evolves
734 through space and time, and factors that influence the distribution of surface ruptures. Studying
735 brittle surface deformation around faults provides useful constraints for seismic hazard
736 assessment. Variations in off-fault damage and fault-zone structure affects the energy available
737 for rupture propagation, thereby infliences the maximum earthquake size and the likelihood of
738 multi-segment ruptures. Moreover, heterogeneous slip distributions and earthquake sized are
739 linked to more irregulat recurrence intervals (e.g. Rodriguez Piceda et al, 2025a,b). Finally, more
740 accurate ground motion preduction equations could account for fault-zone properties, rather

than relying solely on magnitude, distance and soil properties as is commonly done (e.g. (Bommer et al., 2010) Bommer et al., 2010).

5 Conclusions

Our study highlights the importance of progressive brittle deformation in controlling the dissipation of energy along fault planes during shallow earthquake slip. We have identified a four-stage deformation model that explains the progressive development of brittle structures in the upper few hundred meters of the crust by mapping fault plane geometry, on-fault fracture networks, and cross-faults along the Maghlaq and Victoria Lines faults. Our findings demonstrate that on-fault fractures form early but are subsequently modified by cross-faulting, with increased fracture intensity and connectivity near major cross-faults. This suggests that energy dissipation is spatially heterogeneous, with structures such as corrugations and cross-faults causing an increase in the intensity and connectivity of on-fault fractures, and causing the partitioning the seismic energy at different locations on the fault surface over scales of tens of meters. Our results provide insights into how energy dissipation evolves within active fault zones, which has direct implications for seismic hazard assessment.

Acknowledgments

This work was supported by a UKRI Future Leaders Fellowship MR/T041994/1 (PI – Z. Mildon).

Open Research

Spatial analysis was undertaken using Version 3.22 (2022) of QGIS, available from https://qgis.org/download/

Conflict of Interest Disclosure

"The authors declare there are no conflicts of interest for this manuscript."

References

Aki, K. (1984). Asperities, barriers, characteristic earthquakes and strong motion prediction. *Journal of Geophysical Research: Solid Earth*, *89*(B7), 5867–5872. https://doi.org/10.1029/JB089iB07p05867

Allmendinger, R. W., Cardonzo, N. C., & Fisher, D. (2013). *Structural Geology Algorithms: Vectors & Tensors*. Cambridge, UK: Cambridge University Press.

Argnani, A. (1990a). The strait of sicily rift zone: Foreland deformation related to the evolution of a back-arc basin. *Journal of Geodynamics*, *12*(2), 311–331. https://doi.org/10.1016/0264-3707(90)90028-S

Argnani, A. (1990b). The strait of sicily rift zone: Foreland deformation related to the evolution of a back-arc basin. *Journal of Geodynamics*, *12*(2), 311–331. https://doi.org/10.1016/0264-3707(90)90028-S

Barnhart, W. D., Willis, M. J., Lohman, R. B., & Melkonian, A. K. (2011). InSAR and Optical Constraints on Fault Slip during the 2010–2011 New Zealand Earthquake Sequence. *Seismological Research Letters*, *82*(6), 815–823. https://doi.org/10.1785/gssrl.82.6.815

775 Barnhart, W. D., Hayes, G. P., & Gold, R. D. (2019). The July 2019 Ridgecrest, California, Earthquake Sequence:
776 Kinematics of Slip and Stressing in Cross-Fault Ruptures. *Geophysical Research Letters*, *46*(21), 11859–
777 11867. https://doi.org/10.1029/2019GL084741

778 Barth, N. C., Boulton, C., Carpenter, B. M., Batt, G. E., & Toy, V. G. (2013). Slip localization on the southern
779 Alpine Fault, New Zealand. *Tectonics*, *32*(3), 620–640. https://doi.org/10.1002/tect.20041

780 Beeler, N. M., Wong, T.-F., & Hickman, S. H. (2003). On the Expected Relationships among Apparent Stress, Static
781 Stress Drop, Effective Shear Fracture Energy, and Efficiency. *Bulletin of the Seismological Society of*
782 *America*, *93*(3), 1381–1389. https://doi.org/10.1785/0120020162

783 Bommer, J. J., Douglas, J., Scherbaum, F., Cotton, F., Bungum, H., & Fäh, D. (2010). On the Selection of Ground-
784 Motion Prediction Equations for Seismic Hazard Analysis | Seismological Research Letters |
785 GeoScienceWorld. *Seismological Research Letters*, *81*(5), 783–793.
786 https://doi.org/doi.org/10.1785/gssrl.81.5.783

787 Bonson, C. G., Childs, C., Walsh, J. J., Schöpfer, M. P. J., & Carboni, V. (2007). Geometric and kinematic controls
788 on the internal structure of a large normal fault in massive limestones: The Maghlaq Fault, Malta. *Journal*
789 *of Structural Geology*, *29*(2), 336–354. https://doi.org/10.1016/j.jsg.2006.06.016

790 Bradbury, K. K., Evans, J. P., Chester, J. S., Chester, F. M., & Kirschner, D. L. (2011). Lithology and internal
791 structure of the San Andreas fault at depth based on characterization of Phase 3 whole-rock core in the San
792 Andreas Fault Observatory at Depth (SAFOD) borehole. *Earth and Planetary Science Letters*, *310*(1), 131–
793 144. https://doi.org/10.1016/j.epsl.2011.07.020

794 Caine, J. S., Evans, J. P., & Forster, C. B. (1996). Fault zone architecture and permeability structure. *Geology*,
795 *24*(11), 1025–1028. https://doi.org/10.1130/0091-7613(1996)024%253C1025:FZAAPS%253E2.3.CO;2

796 Cardozo, N., & Allmendinger, R. W. (2013). Spherical projections with OSXStereonet. *Computers & Geosciences*,
797 *51*, 193–205. https://doi.org/10.1016/j.cageo.2012.07.021

798 Cello, G., Crisci, G. M., Marabini, S., & Tortorici, L. (1985). Transtensive tectonics in the Strait of Sicily: Structural
799 and volcanological evidence from the Island of Pantelleria. *Tectonics*, *4*(3), 311–322.
800 https://doi.org/10.1029/TC004i003p00311

801 Chester, F. M., & Chester, J. S. (2000). Stress and deformation along wavy frictional faults. *Journal of Geophysical*
802 *Research: Solid Earth*, *105*(B10), 23421–23430. https://doi.org/10.1029/2000JB900241

803 Chester, J. S., Chester, F. M., & Kronenberg, A. K. (2005). Fracture surface energy of the Punchbowl fault, San
804 Andreas system. *Nature*, *437*(7055), 133–136. https://doi.org/10.1038/nature03942

805 Choi, J.-H., Edwards, P., Ko, K., & Kim, Y.-S. (2016). Definition and classification of fault damage zones: A
806 review and a new methodological approach. *Earth-Science Reviews*, *152*, 70–87.
807 https://doi.org/10.1016/j.earscirev.2015.11.006

808 Cocco, M., Aretusini, S., Cornelio, C., Nielsen, S. B., Spagnuolo, E., Tinti, E., & Di Toro, G. (2023). Fracture
809 Energy and Breakdown Work During Earthquakes. *Annual Review of Earth and Planetary Sciences*, *51*(1),
810 217–252. https://doi.org/10.1146/annurev-earth-071822-100304

811 Cowie, P. A. (1998). A healing–reloading feedback control on the growth rate of seismogenic faults. *Journal of*
812 *Structural Geology*, *20*(8), 1075–1087. https://doi.org/10.1016/S0191-8141(98)00034-0

813 Cowie, P. A., Underhill, J. R., Behn, M. D., Lin, J., & Gill, C. E. (2005). Spatio-temporal evolution of strain
814 accumulation derived from multi-scale observations of Late Jurassic rifting in the northern North Sea: A
815 critical test of models for lithospheric extension. *Earth and Planetary Science Letters*, *234*(3), 401–419.
816 https://doi.org/10.1016/j.epsl.2005.01.039

817 Cruikshank, K. M., Zhao, G., & Johnson, A. M. (1991). Analysis of minor fractures associated with joints and
818 faulted joints. *Journal of Structural Geology*, *13*(8), 865–886. https://doi.org/10.1016/0191-
819 8141(91)90083-U

820 Dart, C. J., Bosence, D. W. J., & McClay, K. R. (1993). Stratigraphy and structure of the Maltese graben system.
821 *Journal of the Geological Society*, *150*(6), 1153–1166. https://doi.org/10.1144/gsjgs.150.6.1153

De Paola, N., Bullock, R. J., Holdsworth, R. E., Marco, S., & Nielsen, S. (2025). Off-fault damage controls near-surface rupture behaviour in soft sediments. *Nature Communications*, *16*(1), 11295. https://doi.org/10.1038/s41467-025-66467-4

De Rosa, S. S., Shipton, Z. K., Lunn, R. J., Kremer, Y., & Murray, T. (2018). Along-strike fault core thickness variations of a fault in poorly lithified sediments, Miri (Malaysia). *Journal of Structural Geology*, *116*, 189–206. https://doi.org/10.1016/j.jsg.2018.08.012

Doutsos, T., & Koukouvelas, I. (1998). Fractal analysis of normal faults in northwestern Aegean area, Greece. *Journal of Geodynamics*, *26*(2), 197–216. https://doi.org/10.1016/S0264-3707(97)00052-5

Elliott, J. R., Nissen, E. K., England, P. C., Jackson, J. A., Lamb, S., Li, Z., et al. (2012). Slip in the 2010–2011 Canterbury earthquakes, New Zealand. *Journal of Geophysical Research: Solid Earth*, *117*(B3). https://doi.org/10.1029/2011JB008868

Faulkner, D. R., Lewis, A. C., & Rutter, E. H. (2003). On the internal structure and mechanics of large strike-slip fault zones: field observations of the Carboneras fault in southeastern Spain. *Tectonophysics*, *367*(3), 235–251. https://doi.org/10.1016/S0040-1951(03)00134-3

Ferraro, F., Grieco, D. S., Agosta, F., & Prosser, G. (2018). Space-time evolution of cataclasis in carbonate fault zones. *Journal of Structural Geology*, *110*, 45–64. https://doi.org/10.1016/j.jsg.2018.02.007

Finetti, I. (1985). Structure and Evolution of the Central Mediterranean (Pelagian and Ionian Seas). In D. J. Stanley & F.-C. Wezel (Eds.), *Geological Evolution of the Mediterranean Basin: Raimondo Selli Commemorative Volume* (pp. 215–230). New York, NY: Springer. https://doi.org/10.1007/978-1-4613-8572-1_10

Fletcher, J. B., & McGarr, A. (2006). Distribution of stress drop, stiffness, and fracture energy over earthquake rupture zones. *Journal of Geophysical Research: Solid Earth*, *111*(B3). https://doi.org/10.1029/2004JB003396

844 Friedman, M., & Logan, J. M. (1970). Influence of residual elastic strain on the orientation of experimental fractures
845 in three quartzose sandstones. *Journal of Geophysical Research (1896-1977)*, *75*(2), 387–405.
846 https://doi.org/10.1029/JB075i002p00387

847 Hancock, P. L., & Barka, A. A. (1987). Kinematic indicators on active normal faults in Western Turkey. *Journal of*
848 *Structural Geology*, *9*(5), 573–584. https://doi.org/10.1016/0191-8141(87)90142-8

849 Hill, K. C., & Hayward, A. B. (1988). Structural constraints on the Tertiary plate tectonic evolution of Italy. *Marine*
850 *and Petroleum Geology*, *5*(1), 2–16. https://doi.org/10.1016/0264-8172(88)90036-0

851 Holdsworth, R. E., van Diggelen, E. W. E., Spiers, C. J., de Bresser, J. H. P., Walker, R. J., & Bowen, L. (2011).
852 Fault rocks from the SAFOD core samples: Implications for weakening at shallow depths along the San
853 Andreas Fault, California. *Journal of Structural Geology*, *33*(2), 132–144.
854 https://doi.org/10.1016/j.jsg.2010.11.010

855 Huang, Y. (2018). Earthquake Rupture in Fault Zones With Along-Strike Material Heterogeneity. *Journal of*
856 *Geophysical Research: Solid Earth*, *123*(11), 9884–9898. https://doi.org/10.1029/2018JB016354

857 Hudnut, K. W., Seeber, L., & Pacheco, J. (1989). Cross-fault triggering in the November 1987 Superstition Hills
858 Earthquake Sequence, southern California. *Geophysical Research Letters*, *16*(2), 199–202.
859 https://doi.org/10.1029/GL016i002p00199

860 Ide, S. (2002). Estimation of Radiated Energy of Finite-Source Earthquake Models. *Bulletin of the Seismological*
861 *Society of America*, *92*(8), 2994–3005. https://doi.org/10.1785/0120020028

862 Illies, J. H. (1981). Graben formation — the Maltese Islands — a case history. *Tectonophysics*, *73*(1), 151–168.
863 https://doi.org/10.1016/0040-1951(81)90182-7

864 Jones, L. E., & Hough, S. E. (1995). Analysis of broadband records from the 28 June 1992 Big Bear earthquake:
865 Evidence of a multiple-event source. *Bulletin of the Seismological Society of America*, *85*(3), 688–704.
866 https://doi.org/10.1785/BSSA0850030688

867 Kanamori, H. (2001). Energy Budget of Earthquakes and Seismic Efficiency. In *International Geophysics* (Vol. 76,
868 pp. 293–305). Academic Press. https://doi.org/10.1016/S0074-6142(01)80087-5

869 Kanamori, H., & Rivera, L. (2006). Energy Partitioning During an Earthquake. In *Earthquakes: Radiated Energy*
870 *and the Physics of Faulting* (pp. 3–13). American Geophysical Union (AGU).
871 https://doi.org/10.1029/170GM03

872 Kim, Y.-S., Peacock, D. C. P., & Sanderson, D. J. (2004). Fault damage zones. *Journal of Structural Geology*,
873 *26*(3), 503–517. https://doi.org/10.1016/j.jsg.2003.08.002

874 Lacazette, A. (2009). Paleostress analysis from image logs using pinnate joints as slip indicators. *AAPG Bulletin*,
875 *93*(11), 1489–1501. https://doi.org/10.1306/08110909087

876 Larsen, S., Reilinger, R., Neugebauer, H., & Strange, W. (1992). Global positioning system measurements of
877 deformations associated with the 1987 Superstition Hills Earthquake: Evidence for conjugate faulting.
878 *Journal of Geophysical Research: Solid Earth*, *97*(B4), 4885–4902. https://doi.org/10.1029/92JB00128

879 Lathrop, B. A., Jackson, C. a.-L., Bell, R. E., & Rotevatn, A. (2022). Displacement/Length Scaling Relationships for
880 Normal Faults; a Review, Critique, and Revised Compilation. *Frontiers in Earth Science*, *10*.
881 https://doi.org/10.3389/feart.2022.907543

882 Li, S., Wang, X., Tao, T., Zhu, Y., Qu, X., Li, Z., et al. (2023). Source Model of the 2023 Turkey Earthquake
883 Sequence Imaged by Sentinel-1 and GPS Measurements: Implications for Heterogeneous Fault Behavior
884 along the East Anatolian Fault Zone. *Remote Sensing*, *15*(10). https://doi.org/10.3390/rs15102618

885 Martinelli, M., Bistacchi, A., Balsamo, F., & Meda, M. (2019). Late Oligocene to Pliocene Extension in the Maltese
886 Islands and Implications for Geodynamics of the Pantelleria Rift and Pelagian Platform. *Tectonics*, *38*(9),
887 3394–3415. https://doi.org/10.1029/2019TC005627

888 McKay, L., Lunn, R. J., Shipton, Z. K., Pytharouli, S., & Roberts, J. J. (2021). Do intraplate and plate boundary fault
889 systems evolve in a similar way with repeated slip events? *Earth and Planetary Science Letters*, *559*,
890 116757. https://doi.org/10.1016/j.epsl.2021.116757

McKay, Lucy, Shipton, Z. K., Lunn, R. J., Andrews, B., Raub, T. D., & Boyce, A. J. (2019). Detailed internal structure and along-strike variability of the core of a plate boundary fault: the Highland Boundary fault, Scotland. *Journal of the Geological Society*, *177*(2), 283–296. https://doi.org/10.1144/jgs2018-226

Meng, L., Ampuero, J.-P., Stock, J., Duputel, Z., Luo, Y., & Tsai, V. C. (2012). Earthquake in a Maze: Compressional Rupture Branching During the 2012 Mw 8.6 Sumatra Earthquake. *Science*, *337*(6095), 724–726. https://doi.org/10.1126/science.1224030

Nielsen, S., Spagnuolo, E., Violay, M., Smith, S., Di Toro, G., & Bistacchi, A. (2016). G: Fracture energy, friction and dissipation in earthquakes. *Journal of Seismology*, *20*(4), 1187–1205. https://doi.org/10.1007/s10950-016-9560-1

Okubo, K., Bhat, H. S., Rougier, E., Marty, S., Schubnel, A., Lei, Z., et al. (2019). Dynamics, Radiation, and Overall Energy Budget of Earthquake Rupture With Coseismic Off-Fault Damage. *Journal of Geophysical Research: Solid Earth*, *124*(11), 11771–11801. https://doi.org/10.1029/2019JB017304

Peacock, D. C. P., & Sanderson, D. J. (2018). Structural analyses and fracture network characterisation: Seven pillars of wisdom. *Earth-Science Reviews*, *184*, 13–28. https://doi.org/10.1016/j.earscirev.2018.06.006

Peacock, D. C. P., Sanderson, D. J., & Rotevatn, A. (2018). Relationships between fractures. *Journal of Structural Geology*, *106*, 41–53. https://doi.org/10.1016/j.jsg.2017.11.010

Peacock, D. C. P., Sanderson, D. J., & Magán, M. (2023). Superposed fracture networks. *Geological Magazine*, *160*(9), 1817–1831. https://doi.org/10.1017/S0016756823000730

Pedley, H. M., House, M. R., & Waugh, B. (1976). The geology of Malta and Gozo. *Proceedings of the Geologists' Association*, *87*(3), 325–341. https://doi.org/10.1016/S0016-7878(76)80005-3

Pizzi, A., Di Domenica, A., Gallovič, F., Luzi, L., & Puglia, R. (2017). Fault Segmentation as Constraint to the Occurrence of the Main Shocks of the 2016 Central Italy Seismic Sequence. *Tectonics*, *36*(11), 2370–2387. https://doi.org/10.1002/2017TC004652

914 Ponti, D. J., Blair, J. L., Rosa, C. M., Thomas, K., Pickering, A. J., Akciz, S., et al. (2020). Documentation of
915 Surface Fault Rupture and Ground-Deformation Features Produced by the 4 and 5 July 2019 Mw 6.4 and
916 Mw 7.1 Ridgecrest Earthquake Sequence. *Seismological Research Letters*, *91*(5), 2942–2959.
917 https://doi.org/10.1785/0220190322

918 Putz-Perrier, M. W., & Sanderson, D. J. (2010). Distribution of faults and extensional strain in fractured carbonates
919 of the North Malta Graben. *AAPG Bulletin*, *94*(4), 435–456. https://doi.org/10.1306/08260909063

920 Quye-Sawyer, J., Whittaker, A. C., Roberts, G. G., & Rood, D. H. (2021). Fault Throw and Regional Uplift
921 Histories From Drainage Analysis: Evolution of Southern Italy. *Tectonics*, *40*(4), e2020TC006076.
922 https://doi.org/10.1029/2020TC006076

923 Reuther, C.-D., & Eisbacher, G. H. (1985). Pantelleria Rift — crustal extension in a convergent intraplate setting.
924 *Geologische Rundschau*, *74*(3), 585–597. https://doi.org/10.1007/BF01821214

925 Rezapour, M., & Mohsenpur, A. (2013). The 2010 Mw 6.5 Rigan, Iran, Earthquake Aftershock Sequence. *Bulletin*
926 *of the Seismological Society of America*, *103*(3), 1793–1800. https://doi.org/10.1785/0120120288

927 Rodriguez Padilla, A. M., Oskin, M. E., Brodsky, E. E., Dascher-Cousineau, K., Herrera, V., & White, S. (2024).
928 The Influence of Fault Geometrical Complexity on Surface Rupture Length. *Geophysical Research Letters*,
929 *51*(20), e2024GL109957. https://doi.org/10.1029/2024GL109957

930 Savage, J. C., & Wood, M. D. (1971). The relation between apparent stress and stress drop*. *Bulletin of the*
931 *Seismological Society of America*, *61*(5), 1381–1388. https://doi.org/10.1785/BSSA0610051381

932 Schlische, R. W., & Anders, M. H. (1996). Stratigraphic effects and tectonic implications of the growth of normal
933 faults and extensional basins. In K. K. Beratan (Ed.), *Reconstructing the History of Basin and Range*
934 *Extension Using Sedimentology and Stratigraphy* (p. 0). Geological Society of America.
935 https://doi.org/10.1130/0-8137-2303-5.183

936 Segall, P., & Pollard, D. D. (1983). Nucleation and growth of strike slip faults in granite. *Journal of Geophysical*
937 *Research: Solid Earth*, *88*(B1), 555–568. https://doi.org/10.1029/JB088iB01p00555

938 Shearer, P. M. (2019). *Introduction to Seismology*. Cambridge University Press.

939 Shipton, Z. K., Evans, J. P., Abercrombie, R. E., & Brodsky, E. E. (2006). The missing sinks: Slip localization in
940 faults, damage zones, and the seismic energy budget. In R. Abercrombie, A. McGarr, H. Kanamori, & G.
941 Di Toro (Eds.), *Geophysical Monograph Series* (Vol. 170, pp. 217–222). Washington, D. C.: American
942 Geophysical Union. https://doi.org/10.1029/170GM22

943 Smeraglia, L., Billi, A., Carminati, E., Cavallo, A., & Doglioni, C. (2017). Field- to nano-scale evidence for
944 weakening mechanisms along the fault of the 2016 Amatrice and Norcia earthquakes, Italy.
945 *Tectonophysics*, *712–713*, 156–169. https://doi.org/10.1016/j.tecto.2017.05.014

946 Stein, R. S., & Barrientos, S. E. (1985). Planar high-angle faulting in the basin and range: Geodetic analysis of the
947 1983 Borah Peak, Idaho, earthquake. *Journal of Geophysical Research: Solid Earth*, *90*(B13), 11355–
948 11366. https://doi.org/10.1029/JB090iB13p11355

949 Stein, R. S., King, G. C. P., & Rundle, J. B. (1988). The Growth of Geological Structures by Repeated Earthquakes
950 2. Field Examples of Continental Dip-Slip Faults. *Journal of Geophysical Research: Solid Earth*, *93*(B11),
951 13319–13331. https://doi.org/10.1029/JB093iB11p13319

952 Stewart, I. S., & Hancock, P. L. (1990). Brecciation and fracturing within neotectonic normal fault zones in the
953 Aegean region. *Geological Society, London, Special Publications*, *54*(1), 105–110.
954 https://doi.org/10.1144/GSL.SP.1990.054.01.11

955 Thomas, M. Y., Bhat, H. S., & Klinger, Y. (2017). Effect of Brittle Off-Fault Damage on Earthquake Rupture
956 Dynamics. In *Fault Zone Dynamic Processes* (pp. 255–280). American Geophysical Union (AGU).
957 https://doi.org/10.1002/9781119156895.ch14

958 Torabi, A., Johannessen, M. U., & Ellingsen, T. S. S. (2019). Fault Core Thickness: Insights from Siliciclastic and
959 Carbonate Rocks. *Geofluids*, *2019*, e2918673. https://doi.org/10.1155/2019/2918673

960 Trechmann, C. T. (1938). Quaternary Conditions in Malta. *Geological Magazine*, *75*(1), 1–26.
961 https://doi.org/10.1017/S0016756800089202

962 Villani, F., D'Amico, S., Panzera, F., Vassallo, M., Bozionelos, G., Farrugia, D., & Galea, P. (2018). Shallow high-
963 resolution geophysical investigation along the western segment of the Victoria Lines Fault (island of
964 Malta). *Tectonophysics*, *724–725*, 220–233. https://doi.org/10.1016/j.tecto.2018.01.010

965 Walker, R. T., Bergman, E. A., Elliott, J. R., Fielding, E. J., Ghods, A.-R., Ghoraishi, M., et al. (2013). The 2010–
966 2011 South Rigan (Baluchestan) earthquake sequence and its implications for distributed deformation and
967 earthquake hazard in southeast Iran. *Geophysical Journal International*, *193*(1), 349–374.
968 https://doi.org/10.1093/gji/ggs109

969 Wei, S., Helmberger, D., & Avouac, J.-P. (2013). Modeling the 2012 Wharton basin earthquakes off-Sumatra:
970 Complete lithospheric failure. *Journal of Geophysical Research: Solid Earth*, *118*(7), 3592–3609.
971 https://doi.org/10.1002/jgrb.50267

972 Wesnousky, S. G. (2006). Predicting the endpoints of earthquake ruptures | Nature. *Nature*, *444*, 358–360.

973 Zhang, Y., Tang, X., Liu, D., Taymaz, T., Eken, T., Guo, R., et al. (2023). Geometric controls on cascading rupture
974 of the 2023 Kahramanmaraş earthquake doublet. *Nature Geoscience*, *16*(11), 1054–1060.
975 https://doi.org/10.1038/s41561-023-01283-3

976